

Versatile high resolution crystal spectrometer with x-ray charge coupled device detector

R. Barnsley, N. J. Peacock, J. Dunn, I. M. Melnick, I. H. Coffey et al.

Citation: *Rev. Sci. Instrum.* **74**, 2388 (2003); doi: 10.1063/1.1533105

View online: <http://dx.doi.org/10.1063/1.1533105>

View Table of Contents: <http://rsi.aip.org/resource/1/RSINAK/v74/i4>

Published by the [American Institute of Physics](#).

Related Articles

Study of asymmetries of Cd(Zn)Te devices investigated using photo-induced current transient spectroscopy, Rutherford backscattering, surface photo-voltage spectroscopy, and gamma ray spectroscopies
J. Appl. Phys. **112**, 074503 (2012)

A high resolution gamma-ray spectrometer based on superconducting microcalorimeters
Rev. Sci. Instrum. **83**, 093113 (2012)

Performance of the NIST goniocolorimeter with a broad-band source and multichannel charged coupled device based spectrometer
Rev. Sci. Instrum. **83**, 093108 (2012)

X-ray grating spectrometer for opacity measurements in the 50 eV to 250 eV spectral range at the LULI 2000 laser facility
Rev. Sci. Instrum. **83**, 10E134 (2012)

Quick-scanning x-ray absorption spectroscopy system with a servo-motor-driven channel-cut monochromator with a temporal resolution of 10 ms
Rev. Sci. Instrum. **83**, 083112 (2012)

Additional information on *Rev. Sci. Instrum.*

Journal Homepage: <http://rsi.aip.org>

Journal Information: http://rsi.aip.org/about/about_the_journal

Top downloads: http://rsi.aip.org/features/most_downloaded

Information for Authors: <http://rsi.aip.org/authors>

ADVERTISEMENT



Special Topic Section:
PHYSICS OF CANCER

Why cancer? Why physics? [View Articles Now](#)

Versatile high resolution crystal spectrometer with x-ray charge coupled device detector

R. Barnsley and N. J. Peacock^{a)}

UKAEA/EURATOM Fusion Association, Culham Science Centre, Abingdon, Oxfordshire OX14 3DB, United Kingdom and Department of Pure and Applied Physics, Queen's University of Belfast, Belfast BT7 1NN, United Kingdom

J. Dunn

Department of Physics and Astronomy, University of Leicester, Leicester LE1 7RH, United Kingdom

I. M. Melnick

Department of Physics and Astronomy, University College, London WC1E 6BT, United Kingdom

I. H. Coffey

UKAEA/EURATOM Fusion Association, Culham Science Centre, Abingdon, Oxfordshire OX14 3DB, United Kingdom and Department of Pure and Applied Physics, Queen's University of Belfast, Belfast BT7 1NN, United Kingdom

J. A. Rainnie

Department of Pure and Applied Physics, Queen's University of Belfast, Belfast BT7 1NN, United Kingdom

M. R. Tarbutt

Clarendon Laboratory, University of Oxford, Oxford OX1 3PU, United Kingdom

N. Nelms

Department of Physics and Astronomy, University of Leicester, Leicester LE1 7RH, United Kingdom

(Received 29 October 2002; accepted 4 November 2002)

A family of Johann configuration curved crystal spectrometers has been designed to share the basic engineering features of compactness, modularity, facility of alignment and focus, and incorporation of solid-state charge coupled device detector arrays. These detectors have intrinsically low noise, useful energy resolution, two-dimensional position sensitivity, and readout modes that are programmable. The spectrometers, although relatively compact, with a Rowland circle diameter in the range 0.5–2 m, can still have sufficient resolving power, dispersion, and throughput to be invaluable in high resolution studies of atomic and plasma sources. This article discusses the basic design features and performance of these doubly dispersive spectrometers and illustrates their versatility by applications to studies of a wide range of laboratory x-ray sources such as line emission from highly ionized atoms in the extended plasmas of Tokamaks and nearly point plasmas produced by focused laser irradiation of solids and in beam-foil experiments and electron beam ion traps. © 2003 American Institute of Physics. [DOI: 10.1063/1.1533105]

I. INTRODUCTION

The desirable requirements for x-ray spectrometers used in controlled fusion, mainly Tokamak, research have been outlined by Källne and Källne¹ who also summarize the activity in this field before their publication (1987). Until this date, electronic readout of the spectrum used gas-flow proportional counters, with (“pixel”) spatial resolution $\geq 150 \mu\text{m}$. In order to maintain a high resolving power ≥ 5000 the spectrometers were large, typically with a Rowland circle diameter of several meters,^{2,3} sometimes 10's of meters.⁴ The crystal optic was usually configured to be cylindrical using a four-pillar bending jig, although more inventive methods have been shown to be advantageous. These include the use of differential gas pressure to contour the crystal onto a

former,⁵ or even bending the crystal orthogonal to the dispersion plane as in the von Hámos mode.⁶ The use of double reflection flat crystals⁷ have also been employed in the (1, -1) mode though, in principle, the high resolution (1, +1) mode could have been accessed but at the expense of bandwidth.

At the time of the Källnes' review (1987), charge coupled device (CCD) x-ray detectors were being developed mainly for astrophysical studies. The use of CCDs for direct detection of x rays from laboratory sources, however, has some advantages over more conventional detectors such as gas-flow proportional counters, scintillation converters, microchannel plates, and other solid-state devices. The CCD array is close to the ideal as a two-dimensional (2D) position-sensitive energy-dispersive soft x-ray detector, and has high resolution applications when used in combination with a crystal spectrometer. The spatial resolution, typically $25 \mu\text{m}$, and negligible spatial linearity error are combined

^{a)} Author to whom correspondence should be addressed; UKAEA/EURATOM Fusion Association, Culham Science Centre, Abingdon, Oxfordshire, OX14 3DB, UK; electronic mail: nicol.peacock@ukaea.org.uk

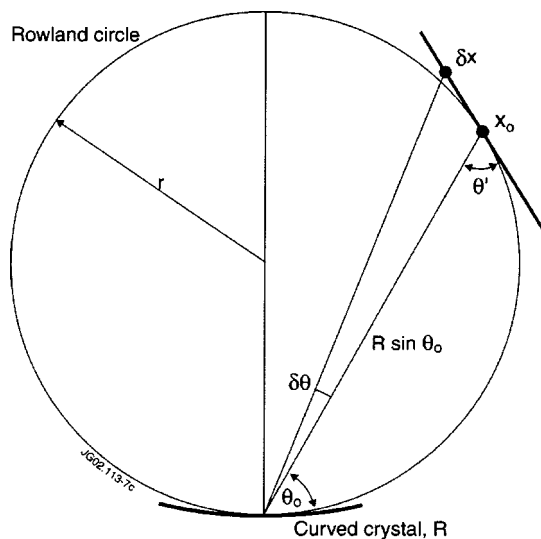


FIG. 1. Johann optical configuration with flat detector plate tangential to the Rowland circle.

with high dynamic range and good intensity linearity. The detector resolution in the case of the CCD offers an improvement of about 1 order of magnitude over conventional multiwire proportional counters. Spectrometers based on CCD detectors can therefore be more compact, maneuverable, and versatile in their range of applications. This can be appreciated, as shown schematically in Fig. 1, from the linear dispersion along a detector plane tangential to the Rowland circle with a diffractor bent to a radius of curvature R , in the Johann optics mode, viz.

$$D = \frac{\delta\lambda}{\delta x} = \frac{2d \cos \theta}{R},$$

where the other symbols have the conventional meaning as in the Bragg relation. The detector-limited resolving power can then be expressed as

$$\frac{\lambda}{\delta\lambda} = \frac{R}{\delta x} \tan \theta,$$

where δx is measured along the detector tangent and is limited by the detector resolution. For a chosen crystal, fixed resolving power and wavelength λ then $R/\delta x$ is a constant. The foregoing assumes that $\delta\theta$ is purely a geometric property of the Rowland circle. In fact $\delta\theta$ is a complicated function of the crystal diffraction profile, which ultimately sets the resolving power, as well as other factors due to the finite dimensions of the crystal and the detector in the Johann configuration and errors due to crystal bending and the quality of the x-ray focus. These limitations^{8,9} on the overall resolution of the present spectrometer are discussed later in the article.

The presently achievable (standard electrode) and projected (open electrode) quantum efficiency of CCD detectors¹⁰ is shown in Fig. 2. Typically, the efficiency is between about 20% and 80% in the energy range from 0.7 to 12 keV, and single photons can be detected with an energy resolution of about 150 eV. A wide range of 1D and 2D readout modes can be accessed, using appropriate software options to read out the x-ray signal electronically in a mode

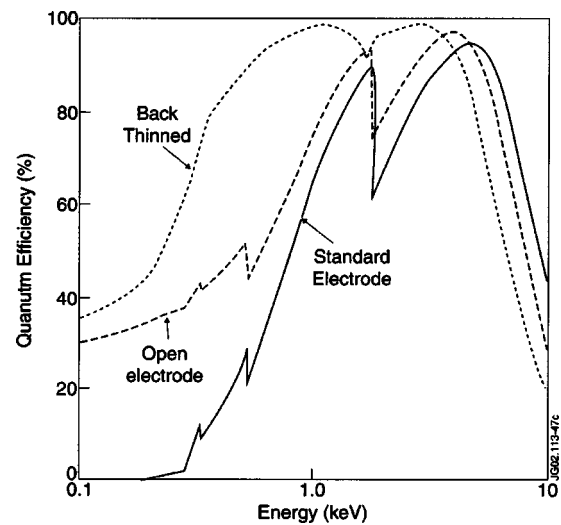


FIG. 2. Quantum efficiency of CCD detectors using high resistivity silicon but with differing electrode structures and electrode materials (poly-silicon), allowing access to lower photon energy (0.1–1.0 keV) (see Ref. 10).

designed to optimize the information from the source. As a secondary advantage, there is no need either for high voltage or high vacuum. The requirement for the array to be cooled below about -30°C , to reduce dark current, is achievable relatively simply, either with liquid nitrogen or thermoelectrically.

The instrument described here has been designed to be sufficiently versatile and portable for use on any of a wide range of plasma, ion-beam, electron-beam, and synchrotron experiments. In most such experiments there is a need to measure absolute and relative wavelengths, line profiles, and lineshifts: features which demand high resolving power and stability. The design aim was for a spectrometer giving access to a wide range of Bragg angles and crystal focal lengths without compromising the mechanical stability between the crystal and the detector. By using the Rowland circle radius as a free parameter, the resolving power need be limited only by the crystal. The large area CCD detector provides an almost ideal complement to its optical characteristics.

The CCD spectrometer, as presently used, has undergone several design modifications during its development, particularly to the crystal holder and to the detector. Early experiments on point sources such beam-foil and laser-produced plasma sources used x-ray film recording, while experiments^{8,11} on the feasibility of using a standard uncooled video readout CCD for plasma x-ray spectroscopy were carried out on DITE¹² (Divertor Injection Tokamak Experiment). These early experiments have led to the use of custom-designed, large area, cooled CCDs which have later found application to the study of the x-ray spectra from JET¹³ (Joint European Torus) and the Oxford electron beam ion trap (EBIT).¹⁴

II. INSTRUMENT DESIGN

Considerations of diverse diffractor use, high resolution, and high light collection, with an $F/\text{no.} = W/R$, where W is the illuminated width of the crystal, favor the Johann optics¹⁵

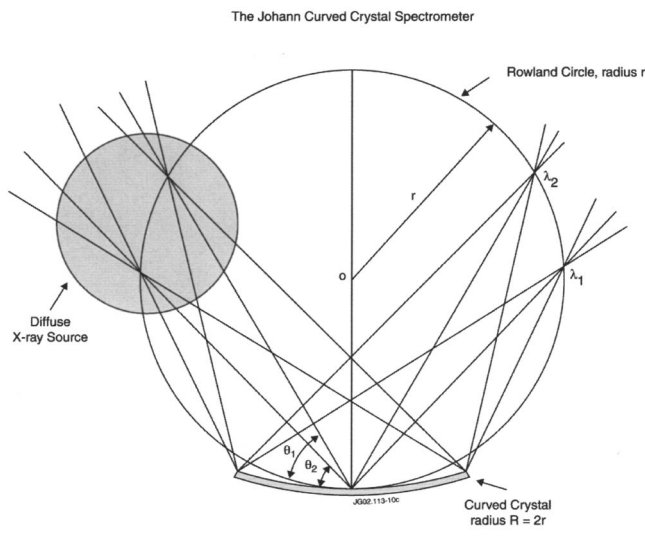


FIG. 3. The Johann curved crystal spectrometer.

as the preferred crystal configuration. In this system, adopted here, the cylindrical crystal is bent to a radius $R = 2r$ and is tangent to the Rowland circle RC at only one point, the crystal pole. Sources either on the Rowland circle or projections of sources through it will be reflected at the appropriate Bragg angle from the illuminated crystal area and focused on the Rowland circle, radius r , on the opposite side of pole as indicated in Fig. 3. As illustrated in Fig. 4, the physical size of the source largely determines its location relative to the dispersion element and this is the main factor in optimizing the waveband, Sec. II D. A position-sensitive detector, tangential to RC at x_o , Fig. 1, is needed to record the focused spectrum.

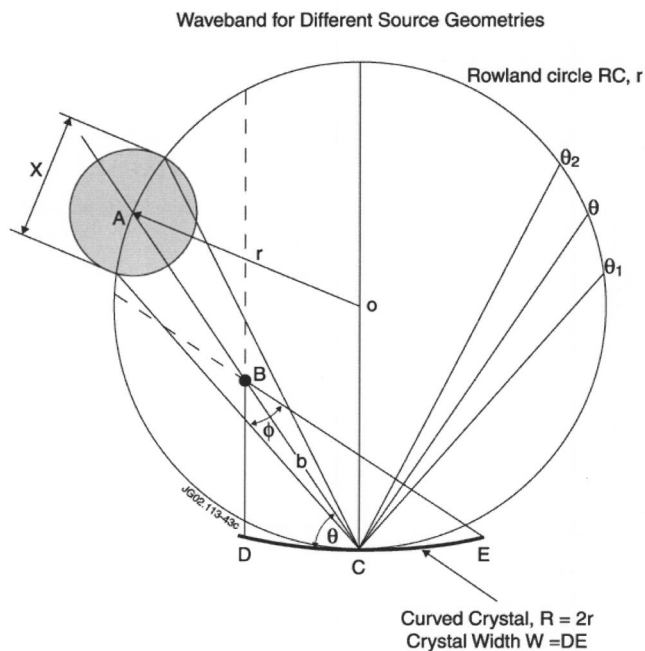


FIG. 4. Optimization of the wave band for different source geometries. The spatial extent x defines the wave band of the diffuse source A located $R \sin \theta$ from the crystal. In order to achieve a useful bandwidth with a point source, B is located inside the Rowland circle.

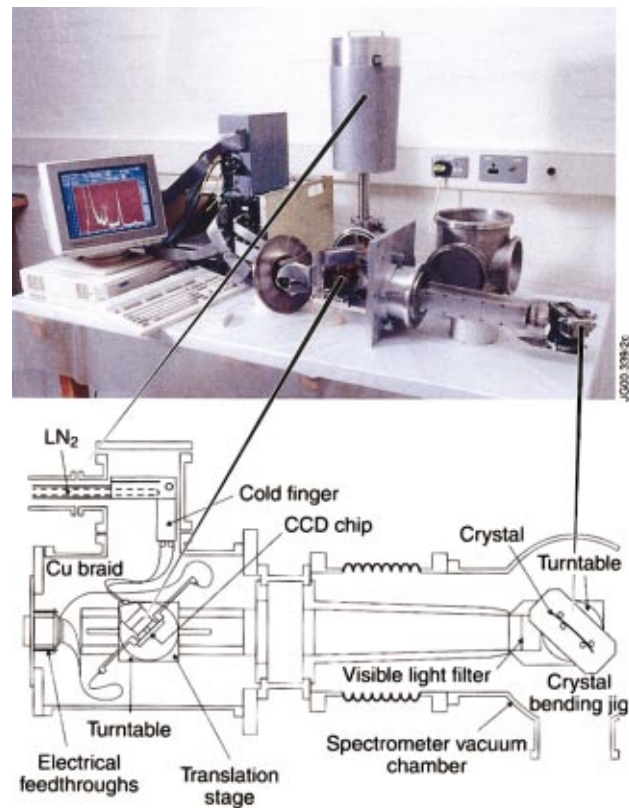


FIG. 5. (Color) A schematic diagram (bottom) of the dispersion arm of the Johann spectrometer with the main components illustrated in the disassembly (top).

A. Engineering layout

The spectrometer was originally designed for a viewing port on the DITE Tokamak where the access was very restricted. Use of an all-encompassing vacuum chamber containing an independent spectrometer structure capable of accessing all reasonable Bragg angles had already been developed and used on DITE but this earlier instrument^{16,17} was not portable and was restricted to RC radii of $r \leq 0.25$ m with consequential bending aberrations.

The salient feature in the design of the present spectrometer is the high stability and versatility achieved by mounting the dispersion arm connecting the crystal and detector to a single rigid beam or “Rowland chord” as illustrated in Fig. 5. This provides a reference axis for all the critical alignments of Rowland circle geometry. The chord length can be varied upwards from about 0.2 m to at least 5 m so as to meet two requirements: first, to adjust the resolving power if this is aberration or detector limited and second, to match the source to the required range of Bragg angles, i.e., to the band pass. At the longer focal lengths, the central section of the chord can be extended by a rigid tube, which also serves as part of the vacuum chamber. The detector–crystal assembly is mounted to the crystal chamber via a flexible bellows, which allows the 2θ angle to be adjusted, while isolating the fixed chord from most of the stresses which would tend to distort the optical axis.

The flexibility of the spectrometer is illustrated in Fig. 6 by the diverse arrangements for viewing a Tokamak plasma. The diffraction arm of the spectrometer, Fig. 5, the ported

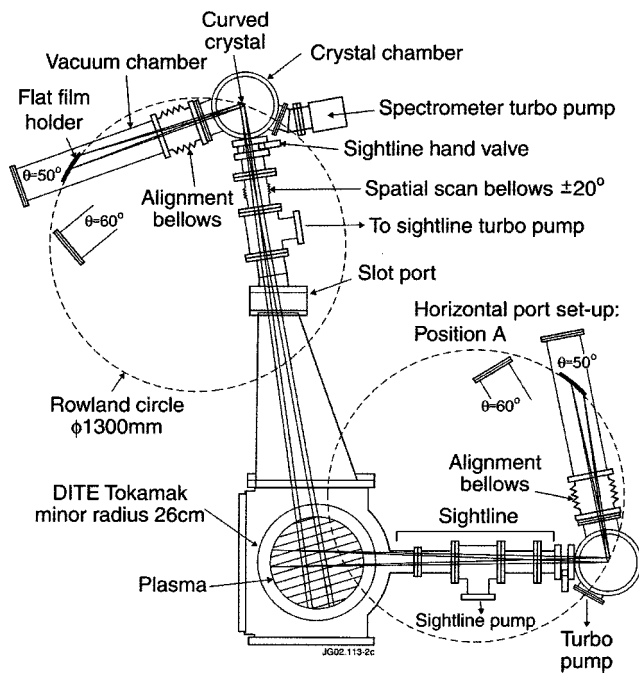


FIG. 6. Vertical and horizontal viewing configurations used on the DITE tokamak.

crystal chamber, and the input arm are component parts of the overall vacuum system shown in Fig. 6.

The crystal chamber itself consists of a cylinder, 250 mm in diameter, with diametrically opposite, 100 mm diam ports. These ports define the input line-of-sight (LOS). The diffraction arm can be coupled to either of two ports, 150 mm in diameter, which are set at 10° and 30° to the orthogonal to the LOS and on the same side of the orthogonal. This immediately gives optional values for the “inclusive angle” φ between the input arm and the diffraction chord of $\varphi = 60^\circ, 80^\circ, 100^\circ,$ and 120° , yielding Bragg angles, depending on the orientation of the chamber, of $\theta_B = 30^\circ, 40^\circ, 50^\circ,$ and 60° , where $\theta_B = (180^\circ - \varphi)/2$. The chamber is built from quickly demountable lightweight (ISO) clamp flanges. At each of these four possible central Bragg angles, rotation about the bellows section allows a $\pm 6^\circ$ Bragg angle range to be accessed, giving a total continuous accessible Bragg angle ranging from 24° to 66° , with overlap between each configuration. The detector is mounted, via a 1 arcmin Vernier rotary table, to a translation stage. This translation stage is long enough to vary the Rowland chord such that a $\pm 6^\circ$ Bragg angle range can be accessed without refocusing the crystal.

The crystal chamber is evacuated by a turbomolecular pump bolted to the unused, 150 mm diam port as in Fig. 6. The sight-line to the Tokamak is pumped separately and isolated from the spectrometer by an unsupported $2 \mu\text{m}$ Mylar window for a waveband $\leq 10 \text{ \AA}$ and a $1 \mu\text{m}$ polypropylene window for a waveband $\geq 10 \text{ \AA}$. Under typical conditions, the sight-line pressure is 10^{-8} Torr and spectrometer chamber pressure is 10^{-6} Torr.

B. Crystal bending jig

The four-pillar crystal bending configuration adopted for the present spectrometer follows the well-established prac-

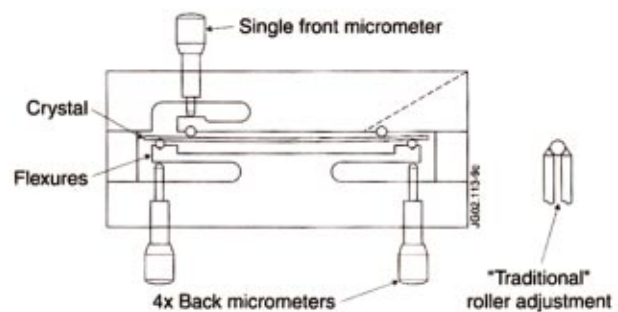
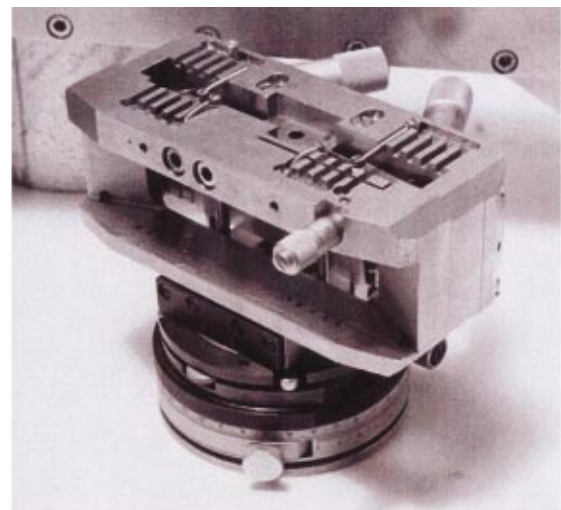


FIG. 7. (Color) Flexure principle of the crystal bending jig (bottom) and photograph of the crystal holder assembly (top).

tice of imposing a cylindrical shape of arbitrary radius on the dispersion element. The crystal jig is mounted, via a 1 arcmin Vernier rotary table, to a two-axis tilt stage that allows small adjustments about the two orthogonal axes perpendicular to the Bragg angle axis. The detailed design of the bending jig,^{8,18} which evolved during an extended program of Tokamak and laser-plasma studies, exhibits some features such as the use of flexures to transfer the loads to the crystal from adjusting micrometers. The use of flexures in the design of the Mark III version, shown in Fig. 7, means that the functions of support and adjustment can be separated and the number of adjusting screws reduced to five. In essence the jig consists of a main massive back body to which is bolted a front clamp face supporting the inner rollers against the illuminated face of the crystal. The single, front micrometer corrects for any residual twist in the front plate by setting both front rollers in the same plane. Once this is set, focusing can take place using the four micrometers and rollers bearing on the back surface of the crystal. This is achieved by a process of iteration using the optical methods described below. Crystals of size up to $100 \times 30 \times 0.5 \text{ mm}^3$ can be bent to a wide range of focal lengths in the range $\sim 0.4 \leftrightarrow \sim 3 \text{ m}$. Details of the materials and tolerances used in the construction of the jig are given in Dunn’s thesis.⁸ Tests of the differential movements of the rollers due to temperature excursions indicated that changes in the crystal curvature are limited to less than $0.5 \text{ mm}^\circ\text{C}$ without loss of focus quality. Thermal stability of the jig was demonstrated during beam-

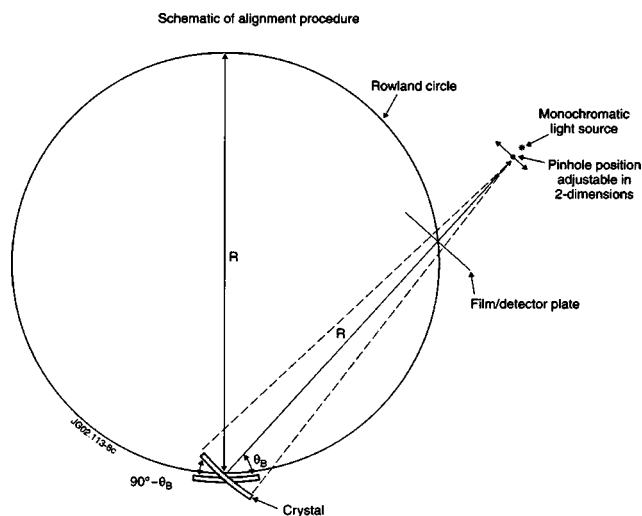


FIG. 8. A schematic diagram of the crystal focusing arrangement using visible light.

foil experiments¹⁹ of Ne x Ly- α using a KAP(002) diffractor with a resolving power of 7×10^3 and integration times of typically 30 h.

C. Focusing and alignment

The crystal is focused and aligned with visible light, using standard optical components mounted on an optical table as illustrated in Fig. 8. The diameter and focus of the Rowland circle are set by triangulation of the source and entrance slit width, the pole of the crystal, and the focused image. A tungsten lamp is used, with a color filter, usually orange or green, to provide a quasimonochromatic light source. This eliminates the confusing multicolored fringes in the image of the source slit, which result from diffraction at the crystal aperture. When adjusting to a curvature >0.5 m radius it is convenient to introduce a reflecting metrology flat into the optical path so that the reflected image is viewed within adjusting distance of the bending jig.

In practice it is normal to start with a wide entrance slit ~ 1 mm which, as the focus is improved, is reduced progressively to $\sim 10 \mu\text{m}$ when the main feature at the eyepiece is the image of the slit convolved with its Fraunhofer diffraction pattern. The sharpness of the image is measurably improved by exclusion of the crystal region in proximity to the front rollers. The width of the central Fraunhofer fringe ω depends on the aperture of the crystal illuminated W , the wavelength λ , and the crystal to the observation plane distance d , viz.

$$\omega = \frac{0.886d\lambda}{W}.$$

Separation of the n th minima is given by

$$S_n = \frac{2nd\lambda}{W},$$

which immediately leads to a useful expression for $\omega = 0.443S_1$ in terms of S_1 , the separation of the first minima in the Fraunhofer diffraction pattern. While Fraunhofer diffraction limits the sharpness of the image, examination of the

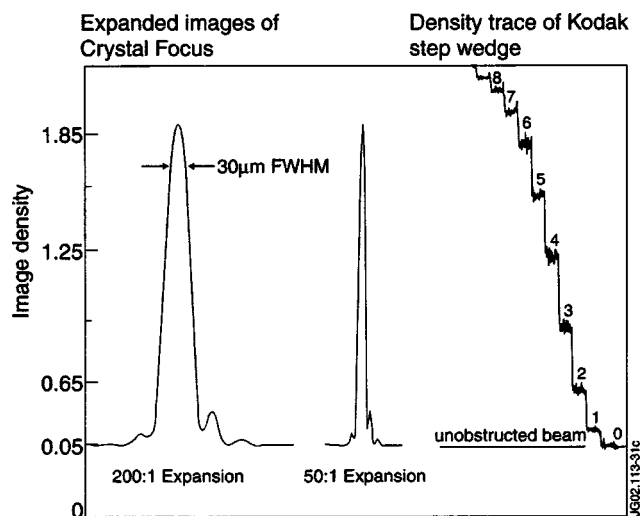


FIG. 9. Results of a calibrated densitometer trace of the optical focus. A FWHM of $30 \mu\text{m}$ over 1 m radius is typical. Photographic density has been converted to light intensity in this illustration. The spatial intensity distribution is close to the theoretical single slit Fraunhofer diffraction pattern.

pattern itself, Fig. 9 can be used to check on the image quality. The exposure leading to the Fraunhofer pattern has been measured on a logarithmic scale using a calibrated photographic emulsion, simply by replacing the eyepiece, Fig. 8, by a 35 mm format camera body. Densitometry of the spatial intensity of the fringe pattern, Fig. 9, shows good agreement⁸ with the theoretical diffraction pattern and indicates an optical focus of the crystal which is correct to 1 part in 50 000.

Alignment of the crystal to the correct Bragg angle as registered on the rotation Vernier is effected first by superimposing cross wires defining the crystal pole with pinhole-projected images of cross wires which define the image at the film holder. This is followed by juxtaposition of the image cross wires and its reflection from the crystal as the Vernier is turned through $90^\circ - \theta_B$, where θ_B is the Bragg angle. Using the present Vernier rotation stage, Bragg angles can be set absolutely to ± 1 arcmin corresponding to an inherent absolute wavelength calibration $\lambda/\delta\lambda = 2000 \rightarrow 5000$. Of course, these procedures involve only visible optics and surface reflections while the true test of the focus and resolving power involves x-ray diffraction.

For the crystals used to date and at the resolving powers $\lambda/\delta\lambda \leq 10^4$ as used in these studies, no correction has been found necessary for any offset between the optical surface and the diffracting planes. In practice, the recorded x-ray spectra often include, or can be superimposed on line features whose absolute wavelengths are sufficiently well known to be regarded as standards and from which the wavelengths of neighboring line features are readily ascertained.

D. Dispersion and bandwidth in Johann configuration

The Bragg relation for diffracted rays along the focal plane tangent, at a distance δx from the fiducial position x_0 , Fig. 1, is given by

$$\lambda = 2d \sin(\theta + \delta x/R),$$

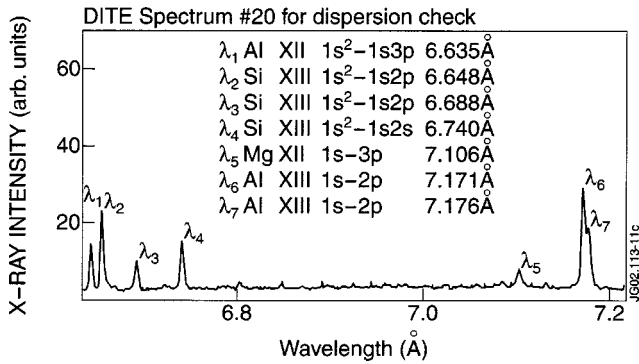


FIG. 10. Spectrum in the 6.6–7.2 Å wave band emitted from the DITE Tokamak recorded on film using an ADP crystal bent to a radius of 1200 mm. The spectrum consists of lines from intrinsic impurity ions of Mg XII, Si XIII, and of Al XII, Al XIII ions produced by laser ablation. The theoretical wavelengths are compared with the values calculated from the dispersion equation in Table II.

where θ_o is the Bragg angle corresponding to x_o . The dispersion relation is given by

$$\delta\theta = \tan^{-1} \left(\frac{\delta x \sin \theta'}{R \sin \theta_o + \delta\theta \cos \theta} \right),$$

where θ' is the angle between the tangent plane and diffraction chord $R \sin \theta_o$. The convention is adopted where δx is positive if it is on the long wavelength side of x_o and negative on the short wavelength side.

A sample spectrum in the spectral region 6.6–7.2 Å, Fig. 10, from ions of intrinsic magnesium, silicon impurities, and laser-ablated aluminum in the DITE Tokamak, is analyzed in some detail to verify the above expression for the spectrometer dispersion. The resolved lines $\lambda_1 \rightarrow \lambda_7$ as well as some adjacent unresolved lines are assigned wavelengths from Drake,²⁰ Mohr,²¹ and Garcia and Mack.²²

The line positions, shown in Table I, were measured on film with a digitized plate reader whose readout accuracy is $\pm 5 \mu\text{m}$. The position of the centroid of the strongest lines approach this tolerance while weaker lines such as λ_5 are measured with a tolerance not exceeding $\pm 20 \mu\text{m}$. The line

centroids shown in column 4 have wavelengths which differ slightly from the theoretical values due to adjustments for the intensities of weaker line blends.⁸

Most of the spectrometer parameters needed in the dispersion relation were determined during the alignment procedure. These include the Roland circle diameter $2r=R=1200 \pm 1 \text{ mm}$, the Bragg angle $\theta_o=40.5^\circ$, and the detector angle tangent to RC , $\theta'=40.5^\circ$. These two angles should be identical to within 1 or 2 arcmin, but they are independent variables and have a different effect on the dispersion function. A literature search for the $2d$ lattice spacing for the synthetic, inorganic crystal used, ADP (101), reveals published values differing by as much as 1 in 500, ostensibly too large a variation for checking the dispersion accuracy. The refractive index correction to the Bragg equation, viz.

$$n\lambda = 2d \left[1 - \left(\frac{2d}{n} \right)^2 \frac{\delta}{\lambda^2} \right] \cdot \sin \theta$$

has also to be considered.

The five parameters R , θ_o , θ' , $2d$, and the refractive index correction $\delta/\lambda^2 = 2.4 \pm 10^{-6} \text{ \AA}^{-2}$, as used in the dispersion relation, have been optimized using a least squared method to give a best fit to the theoretical wavelengths. Table II shows the wavelengths, $\lambda_1, \dots, \lambda_7$, columns 2 and 3, derived from the dispersion relation using both the optimized spectrometer parameters defined in column 1 and their respective measured line positions from Table I. The symbol **F** represents a fixed parameter. This analysis leads to some pertinent observations,⁸ viz.

- (i) the mean wavelength discrepancy from theory is $\overline{\delta\lambda} = 0.17 \text{ m\AA}$, about 25 ppm.
- (ii) The $2d$ spacing, when allowed to vary, consistently gives a value of approximately 10.66 \AA . When held fixed at a mean value of $2d = 10.6402 \text{ \AA}$ suggested in the literature, no minimum in the fitting errors could be found and the resultant wavelength discrepancy is about 2 orders of magnitude higher than (i).
- (iii) A tolerance of $\pm 10\%$ in δ/λ^2 introduces a small change of $\pm 0.015 \text{ m\AA}$ or about 2 ppm in the wavelengths predicted by the dispersion relation.

TABLE I. Theoretical wavelengths and corresponding measured line positions for DITE No. 20. (Note: the superscripts in column 3 are the references numbers to the theoretical wavelengths. The notation (bl)₁₋₄ indicates where the line centroids in column 4 have been adjusted for line blends.⁴)

Line	Identification	Wavelength (Å)	Wavelength (Å)	Position	δx (mm)
λ_1	Al XII $1s^2 \ ^1S_0 - 1s3p \ ^1P_1$	²⁰ 6.634 76	6.634 76	-41.020	± 0.007
	Al XII $1s^2 \ ^1S_0 - 1s3p \ ^3P_1$	²⁰ 6.644 68(bl) ₁			
λ_2	Si XIII $1s^2 \ ^1S_0 - 1s2p \ ^1P_1$	²⁰ 6.647 95(bl) ₁	6.647 95	-39.270	± 0.005
	Si XIII $1s^2 \ ^1S_0 - 1s2p \ ^3P_2$	²⁰ 6.684 99(bl) ₂			
λ_3	Si XIII $1s^2 \ ^1S_0 - 1s2p \ ^3P_1$	²⁰ 6.688 19(bl) ₂	6.688 19	-33.834	± 0.011
	Mg XII $1s \ ^2S_{1/2} - 4p \ ^2P_{3/2}$	²² 6.737 75(bl) ₃			
	Mg XII $1s \ ^2S_{1/2} - 4p \ ^2P_{1/2}$	²² 6.738 19(bl) ₃			
λ_4	Si XIII $1s^2 \ ^1S_0 - 1s2s \ ^3S_1$	²⁰ 6.740 29	6.740 29	-26.782	± 0.005
λ_5	Mg XII $1s \ ^2S_{1/2} - 3p \ ^2P_{3/2}$	²² 7.105 77(bl) ₄	7.106 14	+27.531	± 0.017
	Mg XII $1s \ ^2S_{1/2} - 3p \ ^2P_{1/2}$	²² 7.106 91(bl) ₄			
λ_6	Al XIII $1s \ ^2S_{1/2} - 2p \ ^2P_{3/2}$	²¹ 7.170 91	7.170 96	+37.961	± 0.004
λ_7	Al XIII $1s \ ^2S_{1/2} - 2p \ ^2P_{1/2}$	²¹ 7.176 32	7.176 16	+38.820	± 0.007

^aSee Ref. 8.

TABLE II. Results from optimized dispersion curve.

Parameter in dispersion relation	Parameter values in 7 line fit. $\delta\lambda$ (mÅ) = $\lambda_{\text{theory}} - \lambda_{\text{dispersion}}$		Parameter values in 2 line fit. $\delta\lambda$ (mÅ) = $\lambda_{\text{theory}} - \lambda_{\text{dispersion}}$	
θ_0 (°)	40.55		40.55	
θ' (°)	40.47		40.60	
$2d$ (Å)	10.658 F		10.658 F	
δ/λ^2 (Å ⁻²)	2.40×10^{-6} F		2.40×10^{-6} F	
R (mm)	1199.0		1201.0	
λ_1 (Å) $\delta\lambda_1$ (mÅ)	6.634 80	$\delta\lambda_1=0.04$	6.634 76	$\delta\lambda_1=0.00$
λ_2 (Å) $\delta\lambda_2$ (mÅ)	6.647 95	$\delta\lambda_2=0.002$	6.647 90	$\delta\lambda_2=-0.05$
λ_3 (Å) $\delta\lambda_3$ (mÅ)	6.688 39	$\delta\lambda_3=0.20$	6.688 34	$\delta\lambda_3=0.15$
λ_4 (Å) $\delta\lambda_4$ (mÅ)	6.739 98	$\delta\lambda_4=-0.31$	6.739 93	$\delta\lambda_4=-0.36$
λ_5 (Å) $\delta\lambda_5$ (mÅ)	7.106 36	$\delta\lambda_5=0.22$	7.106 38	$\delta\lambda_5=0.24$
λ_6 (Å) $\delta\lambda_6$ (mÅ)	7.170 86	$\delta\lambda_6=-0.09$	7.170 92	$\delta\lambda_6=-0.04$
λ_7 (Å) $\delta\lambda_7$ (mÅ)	7.176 10	$\delta\lambda_7=-0.06$	7.176 16	$\delta\lambda_7=-0.00$
$\overline{\delta\lambda}$ (mÅ) rms $\{ \cdot (\delta\lambda)^2/n \}^{1/2}$	0.17 mÅ		0.18 mÅ	

The x-ray film spectra thus demonstrate the strength of using the geometrical expression for calculating the dispersion function.

The effect on the recorded bandwidth of source size and position relative to the Rowland circle can best be illustrated using a near-point source such as laser-produced plasma. In such an experiment,²³ a modified version of the Johann spectrometer, with a PET (002), $2d=8.742$ Å crystal, bent to a radius of 300 mm, has been used to record the $n=2$ transitions of He-like and H-like ions of Al in the waveband $7.0 \leftrightarrow 7.9$ Å on a position-sensitive, tangential, film detector. Exposure of the Al target to a single (7 J, 20 ps) laser pulse of $0.52 \mu\text{m}$ irradiation and focal spot size $\phi=50 \mu\text{m}$, is sufficient to generate on Kodak DEF 392 x-ray film, the spectrum shown in Fig. 11. In order to achieve a band pass of say $\lambda/\Delta\lambda_B=10$, the source is required to be located about 90 mm from the pole of the crystal inside the Rowland circle. Thus the spectrometer is used in the “defocused” mode, Fig. 4. It should be noted that in this mode, the increased bandwidth results in a reduction in the monochromatic sensitivity and any given spectral line is reflected from only a fraction of the crystal width. A positive consequence of this, however, is the reduced Johann aberrations, Sec. II E, which allows higher resolving power to be maintained with smaller crystal radii. In the laser-produced plasma experiment the optical focus quality gives a resolution typically better than $\lambda/\Delta\lambda=23\,000$. The overall instrument resolving power is mainly determined by the crystal diffraction width²⁴ of 45 arcsec, corresponding to $\lambda/\Delta\lambda=7000$.

Referring again to Fig. 4, we see that the bandwidth $\Delta\theta$ is the range of angles φ subtended by the crystal width W less the F/no. of the spectrometer

$$\Delta\theta = \theta_1 - \theta_2 = \varphi - \frac{W}{R}.$$

In terms of the Bragg angle, the spatial extent of the source x and the source-to-crystal distance b as in Fig. 4,

$$\Delta\theta = \frac{W \sin \theta}{b} - \frac{W}{R} - \frac{x}{b}.$$

Given the setup parameters for the spectrometer indicated in Table III, the bandwidth (see last row) can be measured directly from Fig. 11 where the extent of the central, diffraction region is bounded at each end by a step in the continuum indicated by an arrow. The measured Bragg angle range $\Delta\theta=0.158$ rad in Table III is in excellent agreement with value derived from the value $\Delta\theta=0.158 \pm 0.006$ rad derived

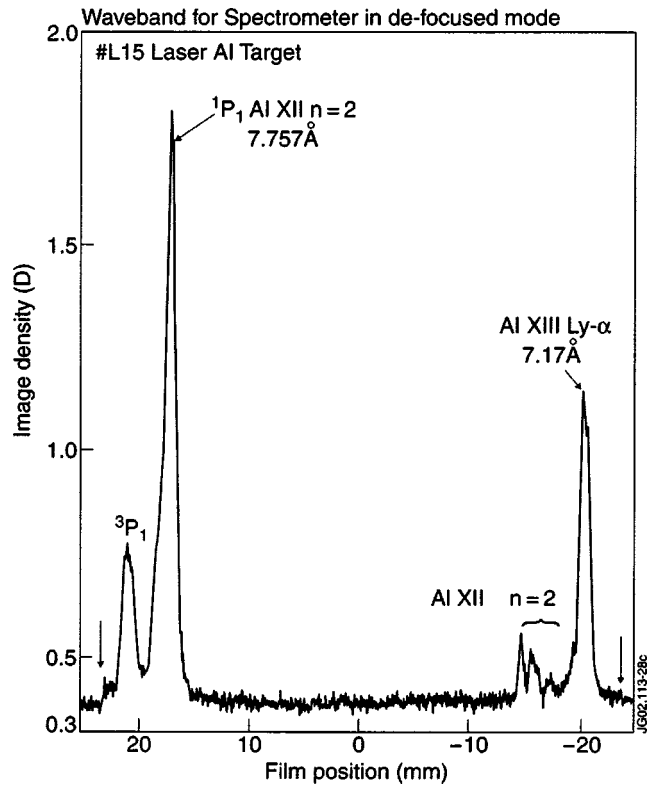


FIG. 11. The recorded waveband from a laser-produced plasma source using the Johann spectrometer in the “defocus” mode. The spectrum is recorded on film from a single (7 J, $\tau=20$ ps, $\lambda=0.52 \mu\text{m}$), laser pulse using a PET(002), $2d=8.742$ Å crystal at a radius of 300 mm. The arrows indicate the wave band limits shown as discontinuities in the continuum intensity. The short wavelength limit is on the “blue” side of the Al XIII Ly- α at 7.17 Å while the long wavelength limit is on the “red” side of the Al XII $2p^3P_1$ intercombination line at 7.80 Å.

TABLE III. Bandwidth verification experiment. The table shows parameters of the Johann spectrometer during exposure to x-ray light from a laser-irradiated Al target.

Radius of crystal curvature	$R = 300$ mm
PET(002) crystal width	$W = 26 \pm 1$ mm
Source-crystal separation	$b = 90$ mm
Mean Bragg angle	$\theta = 59.7^\circ$
Source dimensions	$x = \phi = 50$ μ m
Measured Bragg angle range	$\Delta\theta = 0.158$ rad

from the bandwidth equation immediately above. The main error in the calculation in this case arises from the approximate value of the crystal aperture setting W and not from the finite source size.

E. Instrumental resolving power

Ideally, the instrument broadening function should be measured routinely during an experiment by referring to a fiducial line. Which has inherently low source broadening and lies in the same spectral region as that under study. Such a source might be an electron irradiated gas (Ar) cell.²⁵ In the present applications of the CCD spectrometer, we have of necessity had recourse to a deconvolution of the measured line intensity profile in terms of source and instrument functions. In both the Tokamak and EBIT sources our experience indicates that the minimum source broadening corresponds to an ion energy ≈ 200 eV while instrumental resolving powers in the wavelength region < 10 Å are typically, $\lambda/\Delta\lambda \geq 3000$. Turning our attention to the factors affecting the instrument broadening, the full width half maximum (FWHM) broadening can be expressed equivalently in terms of Δx (pixels), $\Delta\theta$ (rad), or $\Delta\lambda$ (Å) through the relation

$$\frac{\lambda}{\delta\lambda} = \frac{R}{\Delta x} \tan \theta \sin \theta = \frac{\tan \theta}{\Delta \theta}$$

The main factors affecting the instrument broadening are the crystal rocking curve,²⁶ the FWHM of which is denoted by $\bar{\omega}_x$ (rad) while the integrated area or reflectivity under this curve is R_c (rad),

$$R_c = \int_0^{\pi/2} P_\lambda(\theta) d\theta,$$

where $P(\theta)$ is the Prins function.²⁶ While model calculations of crystal rocking curves exist for most diffractors, the actual sample and its bending configuration will determine the practical value of $\bar{\omega}_x$. In general in this study, experimentally derived widths from two-crystal diffraction profiles are preferred.^{24,27} The effect of bending the crystal is to strain the lattice spacing. This imposed distortion to the $2d$ value is greatest¹⁸ for high photon energy and a low- Z crystal with a tightly bent radius. For Si(440), 12 keV x rays and $R = 300$ mm, $\delta(2d)/2d = 10^{-4}$. The reflection integral and the diffraction width are also increased^{28,29} at such tight radii.

In addition we have a small correction $\Delta\theta_R$ to the Bragg angle due to the refractive index of the crystal, where $\delta = \Delta\theta_R \sin \Delta\theta_B \cos \Delta\theta_B$ and the refractive index⁸ parameter δ is incorporated in the Bragg relation

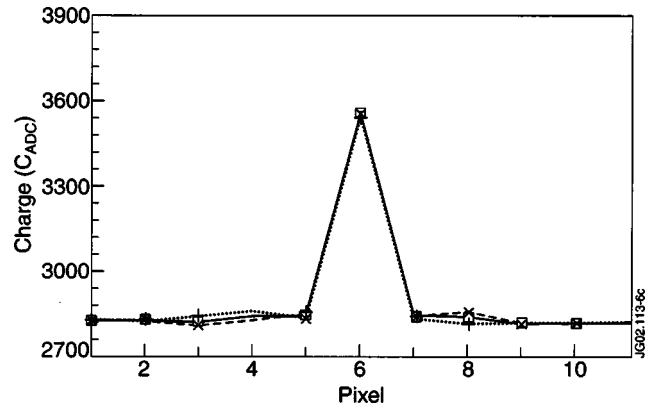


FIG. 12. Charge spreading in the CCD array measured with an ⁵⁵Fe source. An area of 11×11 pixels is examined around any one pixel containing charge. The numbers shown are an average using this procedure over the whole CCD chip.

$$n\lambda = 2d \left[1 - \left(\frac{2d}{n} \right)^2 \frac{\delta}{\lambda^2} \right] \sin \theta.$$

Apparent line broadening due to the finite element size Δx_D of the detector (22.5 μ m) is given by

$$\Delta\theta_D = \frac{\Delta x_D}{R \sin \theta_B}.$$

The actual CCD detector element size adopted in these experiments is 2×22.5 μ m in the dispersion plane and 1×22.5 μ m in the orthogonal plane. Charge spreading across the pixels has been investigated by irradiating the chip with a ⁵⁵Fe source, excluding multiphoton events and averaging any charge accumulation in neighboring pixels over the whole CCD area. The resultant point-spread function is shown in Fig. 12 and can be seen to have negligible charge spreading with a half width of 1 pixel.

The instrument broadening can be thought of as a convolution of the crystal broadening, broadening due to the finite element size Δx_D of the detector, and aberrations due to the Johann geometry and misalignments. The total instrument function is a complex convolution of

$$\Delta\theta(\text{instr.}) = F\{\bar{\omega}_x + \Delta\theta_D + [\Delta\theta_W + \Delta\theta_H + \Delta\theta_6 + \Delta\theta_7]\},$$

where $\Delta\theta_D$ is the detector broadening, $\Delta\theta_W$ and $\Delta\theta_H$ are the Johann aberrations due to the crystal width and height, $\Delta\theta_6$ is the error due to the tangential detector meeting the RC at only one point, and $\Delta\theta_7$ is due to displacement Δd of the detector plane from the crystal-detector chord $d = R \sin \theta$. We have for the Johann aberration $\Delta\theta_W$ due to the crystal not being in contact with the RC throughout its whole width W :

$$\Delta\theta_W = \frac{W^2}{8R^2 \tan \theta_B}.$$

The Johann height error $\Delta\theta_H$ due to the superposition of a series of parabolic line foci displaced vertically³⁰ is perhaps more serious for extended sources like Tokamaks but can be written as

$$\Delta\theta_H = \frac{H^2}{8R^2 \sin \theta_B \cos \theta_B}$$

with the assumption that the detector, crystal, and source are all of the same height H . The error $\Delta\theta_6$ due to the detector plane being in contact with the RC only at the detector pole is greatest at the position x of the longest and shortest wavelengths in the waveband and is given by

$$\Delta\theta_6 = \frac{x^2 W}{8R^3 \sin^2\theta_B}$$

Finally a defocusing error $\Delta\theta_7$ will occur if the detector plane is displaced by Δd from the detector pole, which lies along the diffraction chord at $R \sin\theta_B$ from the crystal pole

$$\Delta\theta_7 = \frac{\Delta d W}{R^2 \sin\theta}$$

Using the above as a starting point and assuming that we are using a Si(111),³¹ $2d = 6.271 \text{ \AA}$, crystal diffraction in first order, we can construct a realistic estimate of the overall instrument resolving power using the following parameters: $R = 1300 \pm 1 \text{ mm}$; $W \times H = 20 \times 15 \text{ mm}$; $x = 90 \text{ mm}$; $\Delta x_D (1 \text{ pixel}) = 22.5 \text{ \mu m}$; and $\theta_D = 50 \pm 0.167^\circ$. Then, we have the following defocusing errors:

$\bar{\omega}_x$	crystal broadening	$\lambda/\Delta\lambda_x = 8.0 \times 10^3$
$\Delta\theta_D$	detector resolution	$\lambda/\Delta\lambda_D = 5.0 \times 10^4$
$\Delta\theta_W$	Johann width error	$\lambda/\Delta\lambda_W = 4.8 \times 10^4$
$\Delta\theta_H$	Johann height error	$\lambda/\Delta\lambda_H = 3.5 \times 10^4$
$\Delta\theta_6$	detector tangent extremity	$\lambda/\Delta\lambda_6 = 1.6 \times 10^4$
$\Delta\theta_7$	radius setting error	$\lambda/\Delta\lambda_7 = 3.2 \times 10^4$
$\Delta\theta_B$	Bragg angle misalignment	$\lambda/\Delta\lambda_B = 1.3 \times 10^4$
$\Delta\theta_R$	refractive correction	$\lambda/\Delta\lambda_R = 5.8 \times 10^4$

From the above it can readily be appreciated that the detector broadening and the Johann aberrations are small fractions of the total instrument function. The crystal diffraction width and accumulated errors in setting up the crystal optics will account approximately for the resolving powers.

Over a series of experiments, using a Tokamak extended source, the instrument broadening was de-convolved as described in the following section from the x-ray line data with the help of analytic routines. The spectral line intensity distribution can be described by a convolution of a Gaussian $G(x-y)$ and a Lorentzian function $L(y)$, resulting in a Voigt function $V(x, \eta)$, where x, y are energy or wavelength displacements about the line centroid and η is the ratio of the component linewidths $\eta = \Delta\lambda_{\text{GAUSSIAN}}/\Delta\lambda_{\text{LORENTZ}}$:

$$V(x, \eta) = \int_{-\infty}^{\infty} L(y)G(x-y)dy$$

A tabulation, accurate to better than 1 in 10^4 , has been calculated by Davies and Vaughan³² and describes the Voigt profile

$$V(x, \eta) = \frac{1}{\eta\sqrt{\pi}} \int_{-\infty}^{\infty} \frac{\exp\{-[(x-y)/\eta]\}^2}{1+y^2} dy$$

as a series of widths as fractions of the FWHM at various intensities over the a range of $0.1 \leq \eta \leq 10$ in logarithmic intervals. The Lorentzian function $1/(1+x^2)$ whose FWHM $\delta_L = 2$ units has been convolved with the Gaussian function $(\eta\sqrt{\pi})^{-1} \cdot \exp[-(x/\eta)^2]$ whose FWHM is $\delta_G = 2\eta(\log_e 2)^{1/2}$ units. When $\eta = 0$ the Voigt function is purely Lorentzian

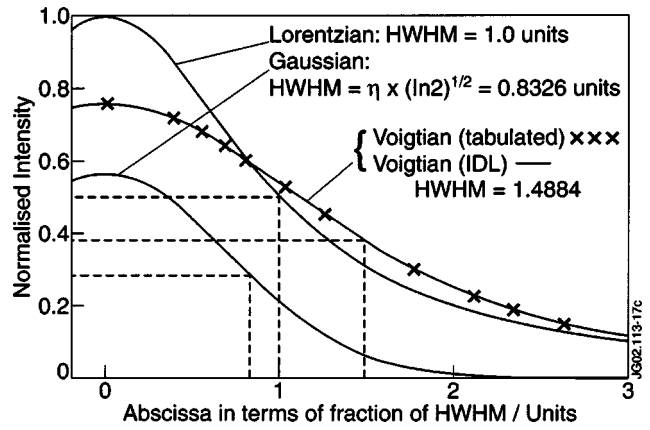


FIG. 13. Deconvolution of analytical $\eta = 1.00$ Voigt profile into Lorentzian and Gaussian components. Also shown is the re-convolution of these components using an independent IDL routine (IDL is a trademark of Research Systems Inc.).

while if $\eta = \infty$ the function is Gaussian. A reconstruction from the D and V^{32} tables of the Voigt function and the component profiles for the particular case of $\eta = 1$ is shown in Fig. 13. As a check, the component functions have been reconvolved using an IDL routine to construct the original Voigtian. An operational difficulty with the D and V^{32} tables is the computational time required to reconstruct the experimental profiles in terms of the tabulated functions. A number of analytical representations of the true Voigt function or psuedo-Voigt functions have been developed to overcome the fitting time. In this work the psuedo-Voigt expression³³

$$V(\lambda, a) = \frac{V_0}{\left[1 + (2a^2 - 1) \left(2 \frac{\lambda - \lambda_0}{\Delta\lambda}\right)^2\right]^{1/a^2}}$$

has been used. When the parameter $a = 1$ then the function is purely Lorentzian and when $a \rightarrow 0$ we have a Gaussian. A least squares fit of $V(\lambda, a)$ to the profile data in terms of the peak intensity V_0 , width $\Delta\lambda$, and centroid position yields a . Having previously established a working relation^{9,34} between a and η the components of the Voigtian is then derived from the D and V^{32} tables. The Gaussian component is identified with the source function which in high temperature plasma sources is due mainly to Doppler motion while the Lorentzian is identified with the instrument resolution. This latter assumption is strictly only true for perfect crystals and in the limit of total absorption.²⁶

Using the above procedure, analysis of the C1 XVI $1s^2 1S_0 - 1s2p^1P_1$ line at 4.4436 \AA from the COMPASS Tokamak and with a Si(111) crystal and $\theta_B = 45^\circ$ can be compared with the resultant resolving power of the putative list of defocusing errors with $\theta_B = 50^\circ$ shown above. A simple addition of the broadening factors, all assumed Lorentzian, would give $\lambda/\Delta\lambda_1 = 2.615 \times 10^3$ while if assumed Gaussian and summed in quadrature $\lambda/\Delta\lambda_1 = 5.94 \times 10^3$ compared with the derived value of between 3.3×10^3 and 3.5×10^3 , shown in Table IV.

At longer wavelengths and larger θ_B , line emission from lighter ions, e.g., Ne x Ly- δ affords better resolution, proportional to $\tan\theta_B/\sqrt{M}$, where M is the ion mass, in the measure-

TABLE IV. Results of fitting procedure to Cl xvii line at 4.4436 Å from the COMPASS Tokamak using a Si(111) crystal.

Parameter	Lower limit	Upper limit
a	0.85	0.80
η	1.0	1.11
$\delta/2$ /units	1.4884	1.5701
ΔL /mÅ	1.34	1.27
ΔG /mÅ	1.12	1.18
$\lambda/\Delta\lambda_1$	3311	3496
T_i /(eV)	380.2	423.6

ment of source broadening of Tokamak spectra. Neon-injected COMPASS-D spectra taken with an ADP diffractor are shown in Fig. 14. The neon line is demonstrably broader than the neighboring metallic lines. A Voigt analysis of the identified lines is summarized in Table V. The instrument resolving power $\lambda/\Delta\lambda_1 \approx 3\,300$ while ion temperatures, very reasonably in the region 350–600 eV in ohmic heated conditions, depend on their location within the plasma volume.

An alternative attempt to measure the instrument width using the properties of a Tokamak source is illustrated in Fig. 15 where the pseudo-Voigt parameter a is plotted against the experimental line widths expressed as $\lambda/\Delta\lambda_{\text{EXP}}$. The 5.038 Å line of S xv and a Si(111) diffractor are chosen for this experiment which consists of measuring linewidths over a wide range of plasma conditions and in particular, electron density. At the lowest extremity of density $n_e \leq 1 \times 10^{19} \text{ m}^{-3}$, in ohmic, or electron cyclotron resonance heated discharges, collisional coupling between the hotter electron and cooler ion fluids is weakest and source broadening of the ions is at a minimum. The experimental line width is then dominated by instrument broadening with an approximation to a Lorentzian profile and $a \rightarrow 1$. Extrapolation to $a=1$ in Fig. 15 indicates values for $\lambda/\Delta\lambda_1 = 2.6 \times 10^3$.

The resolution of the instrument is improved over that obtainable with Tokamaks if the emission is from a point source on or near the Rowland circle.¹⁴ The diffracted image width is the larger of the source size or the Johann defect. In this context a “large” source, size x_s , is obtained when $x_s/R \sin \theta > \Delta\theta_w$. The following two experiments have demonstrated such an improvement. The best resolving power, to date, at wavelengths above 10 Å has been demonstrated^{8,19} with Ne X ions produced in a beam-foil source by stripping a beam of 39 MeV Ne⁶⁺ ions in a 0.5 μm carbon foil, at the Oxford University Folded Tandem accelerator. For this experiment the instrument was positioned downstream of the ion source and the emission observed along the beam axis. This viewing direction, the first axial observation of such a source, was chosen to minimize Doppler broadening due to ion beam divergence coupled with the finite instrument F/no.. The resulting Ne X Lyman- $\alpha_{1,2}$ spectrum, Fig. 16, was recorded during a 30 h exposure on photographic film, using a KAP(002) crystal with $2d=13.16$ Å, bent to a radius of 1073 mm. The experimental resolving power $\lambda/\delta\lambda = 4400$ is a convolution of both source and instrument broadening and is about a factor of 2 lower than the calculated single-crystal

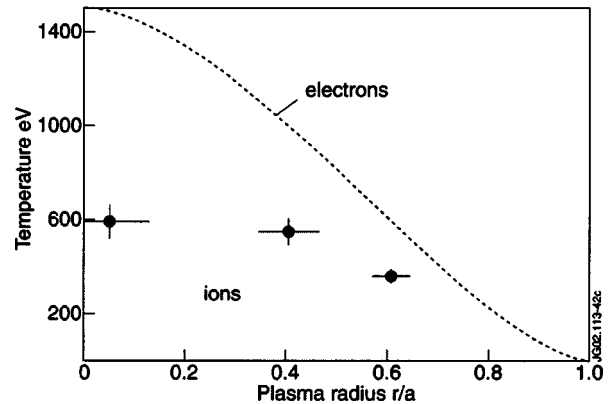
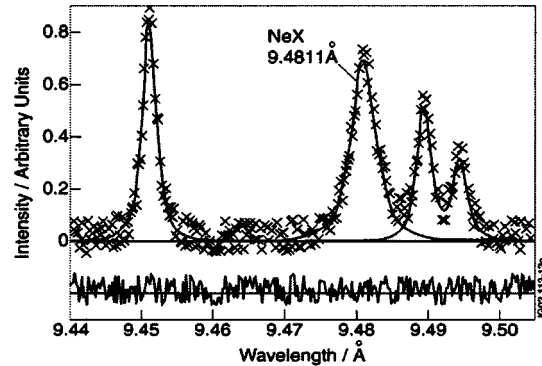
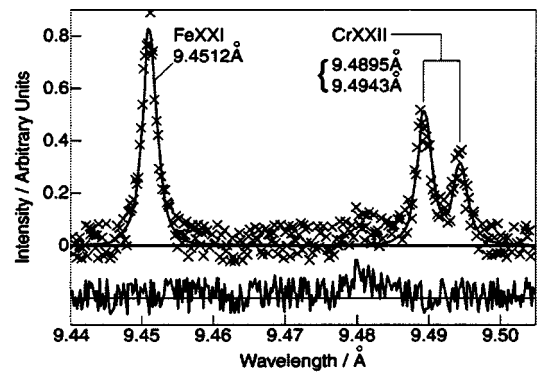


FIG. 14. Results of Voigt fitting procedure to COMPASS Tokamak discharge No. 26354 with neon injection at $t = 170$ ms. The upper spectrum is at a time prior to neon injection while the lower spectrum is taken after neon injection. The Ne X Ly- δ line profile is noticeably wider than those of the metal lines. The bottom graph compares the electron temperature from Thomson scattering with the ion temperature corresponding to each ion, its locality in the minor plasma radius having been calculated using a transport code.

value. If recorded from a plasma this would be equivalent to an ion temperature of about 180 eV.

In some very recent applications^{14,35} of the present spectrometer to high resolution measurements of $n=1-2$ transitions in He-like Ar¹⁶⁺ and H-like Ar¹⁷⁺ in the Oxford EBIT, a fractional precision of 25 ppm has been achieved with a Si(111) crystal diffractor and CCD detection. These experiments³⁵ are sufficiently accurate to discriminate between the energies of the $1s^2 2s-1s 2s 2p$ and $1s^2 2p-1s 2p^2$ Ar¹⁵⁺ transitions satellite to the $n=2$ resonance wavelengths in Ar¹⁶⁺ predicted by the various existing theoretical models.

TABLE V. Results of fitting procedure to line spectra in vicinity of Ne x Ly- δ using an ADP crystal and $RC = 987$ mm. The symbols a and η are the fitting parameters to the pseudo-Voigt and Voigt functions, respectively. The experimental widths and the derived spectrometer resolving powers are given by $\Delta\lambda_{\text{FWHM}}$ and $\lambda/\Delta\lambda_1$. The Gaussian source temperature is tabulated with the location r/a of the peak of the ion emission measured along the minor Tokamak radius.

Ion	λ (\AA)	$\Delta\lambda_{\text{FWHM}}$ (m \AA)	a	η	$\lambda/\Delta\lambda_1$	T_i (eV)	Error (eV)	r/a
Ne x	9.4811	4.00	0.78	1.25	3309.9	360.6	± 50	0.65
Fe XXI	9.4512	2.32	0.80	1.00	3362.2	582.1	± 100	0.4
Cr XXII	9.4895	2.37	0.80	1.11	3209.3	589.9	± 100	0.3

In tests of the ultimate resolution of the spectrometer to a ‘‘point’’ source, $x_s = 100 \mu\text{m}$, the Ly $\alpha_{1,2}$ doublet of A^{17+} has been recorded with the EBIT source placed on or near the Rowland circle at a Bragg angle $\theta = 36.55^\circ$ and with a radius of curvature of 1349 mm, and a clear aperture between the rollers of the crystal bender of 40 mm. The CCD detector is placed tangential to the Rowland circle. Sample spectra obtained both with a Si(Li) detector and the crystal spectrometer are shown. Although the sample spectra shown is the sum over several different 20 min exposures, the high resolution in Fig. 17 is immediately evident with the two Lyman- α lines very well resolved. The line profiles are to a good approximation, Gaussian. In order to study in more detail the line shape the spectrometer has been arranged to view only the $2p_{3/2} - 1s_{1/2}$ transition in Ar^{17+} , with the source very close to the Rowland circle. An example spectrum obtained with such a setup is shown in Fig. 18 along with a Gaussian fit both to the data and to the deconvolved source line profile. The effect of anisotropic emission from the source and the different response of the crystal to π and σ polarizations are handled by the calculation¹⁴ of two sepa-

rate, predetermined rocking curves, one for each direction of polarization. The sum of these π and σ curves for Si(111) at the Lyman- α centroid of 3.734\AA has a width of approximately 0.09 mrad, implying a crystal resolving power of 8300. The instrument function Fig. 18(b) is a purely theoretical construct of a ray tracing code³⁶ ‘‘Virtual Johann.’’ In the calculation of this point-spread function, emission from an arbitrary source point is traced via an arbitrary point on the crystal to the detector co-ordinate determined by Bragg reflection and the process repeated for all points across the crystal width and for representative emissions from an assumed Gaussian intensity source. The code then builds up an intensity distribution at the detector, typically using 50 000 rays per wavelength. The spectrometer line shape is then deconvolved from the raw data using a numerical deconvolution algorithm^{37,38} resulting in the source line profile shown in Fig. 18(c). The FWHM of the fitted Gaussian implies a Doppler limited resolution of $\Delta\lambda/\lambda = 3.3 \times 10^{-4}$ and an equivalent ion temperature of 734 eV. The overall instrument resolving power, Fig. 18(b), is calculated to be

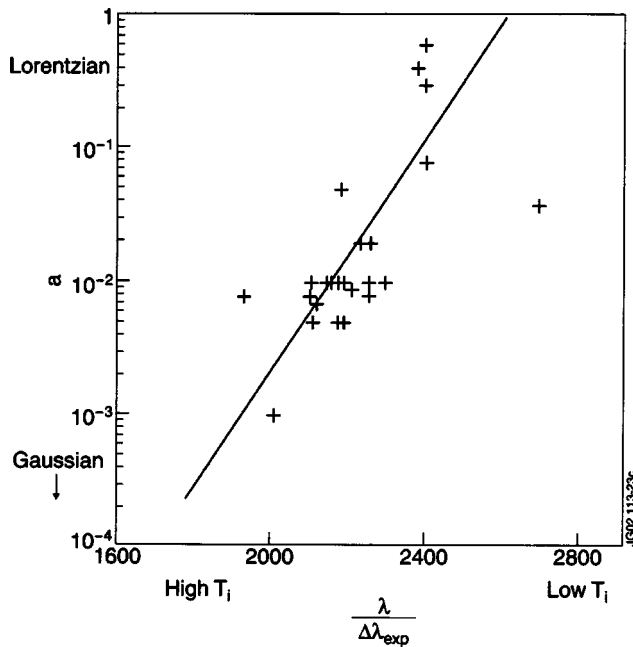


FIG. 15. Fit to pseudo-Voigt function of full half widths $\Delta\lambda_{\text{EXP}}$ of S XV $1s^2 - 1s2p$ ‘w’ line at 5.038\AA , {Si (III) crystal, $R = 1027$ mm, $\theta_B = 54^\circ$ }. The derived a parameter is plotted for several shot numbers over a wide range of COMPASS plasma densities. In the limit as $a \rightarrow$ unity, the function is Lorentzian and $\lambda/\Delta\lambda_{\text{EXP}}$ approximates to the instrument resolving power.

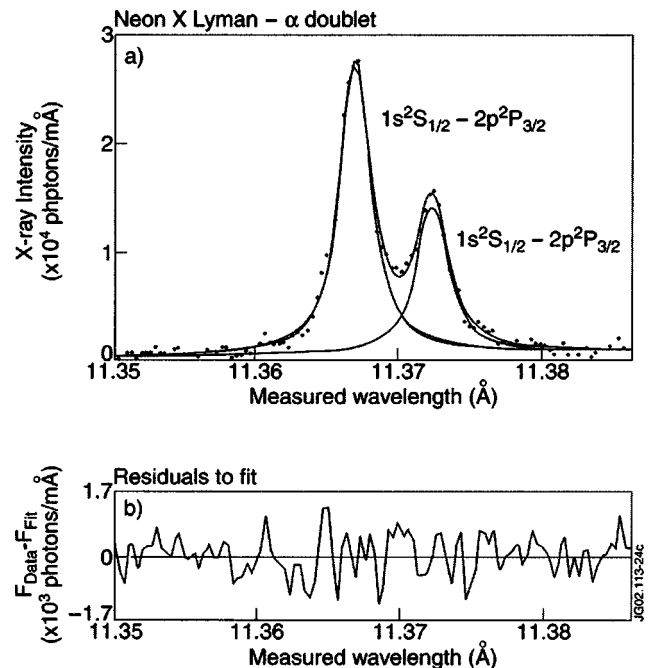


FIG. 16. Neon x Ly- α_1, α_2 spectrum integrated on film over 31 h exposure to a neon beam-foil source using a KAP (002) crystal in the Johann spectrometer. The measured wavelengths are Doppler shifted to 11.37\AA from 12.13\AA due to the viewing angle relative to the beam direction.

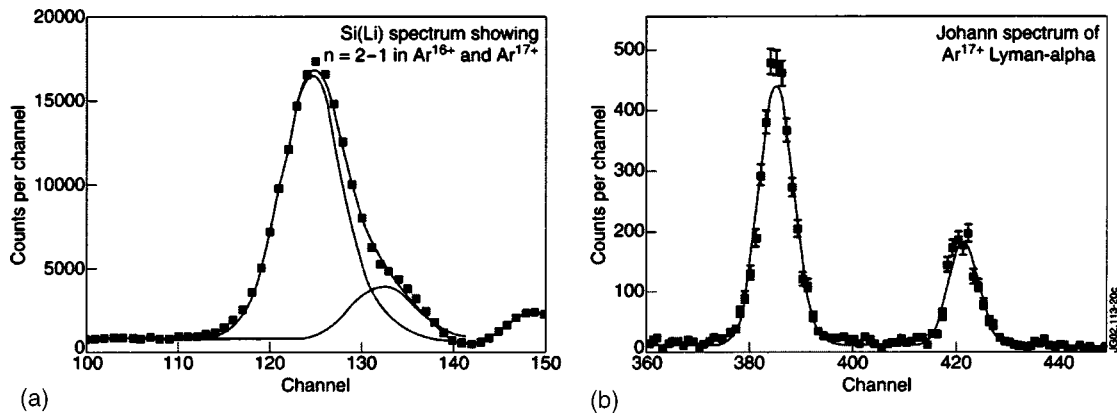


FIG. 17. (a) EBIT spectrum of $n=2-1$ transitions in Ar^{16+} and Ar^{17+} using Si(Li) detector and an exposure time of 5 min. (b) Johann CCD spectrum of the same EBIT source using Si(111) crystal and 2 h exposure. The “best fit” continuous lines shown are Gaussian.

$\lambda/\Delta\lambda_{INST}=7600$, which is not far short of the theoretical crystal resolving power itself.

F. Spectrometer efficiency

The theoretical efficiency of the spectrometer for a given experiment can be expressed as

$$\epsilon = \frac{\Omega}{4\pi} \epsilon_{CRYSTAL} \epsilon_{CCD} T_{WINDOW},$$

where, $\Omega/4\pi$ is the solid angle accepted by the spectrometer, $\epsilon_{CRYSTAL}$ is the crystal reflectivity determined by the rocking curve profile, ϵ_{CCD} is the quantum efficiency of the CCD detector, and T_{WINDOW} is the transmission of the Be or other window. The fact that the x rays are focused in the horizontal plane but continue to diverge in the vertical plane has to be taken into account, so Ω becomes

$$\Omega = \frac{W_{CRYSTAL}}{L_{CRYSTAL}} \frac{H_{DETECTOR}}{L_{TOTAL}},$$

where $W_{CRYSTAL}$ and $L_{CRYSTAL}$ are, respectively, the crystal width and its distance from the source, while $H_{DETECTOR}$ is the height of the detector and L_{TOTAL} is the total path length between the source and detector via the crystal.

Applying these expressions to the EBIT experiment illustrated in Fig. 17, we can evaluate ϵ for the spectrometer by comparing the CCD charge with the signal from the calibrated Si(Li) detector. The total count rate of the Si(Li) detector due to the two Lyman- α lines is $93.6 \pm 1.6 \text{ s}^{-1}$ with a detection efficiency of 3.56×10^{-5} . Over a 20 min period, the average spectrometer count rate from the integrated Lyman- α lines is $1.07 \pm 0.03 \text{ s}^{-1}$, yielding an overall spectrometer efficiency of 4.1×10^{-7} . A simulation of the experimental setup gives an effective crystal efficiency using the “virtual Johann” code of $\epsilon_{CRYSTAL}=0.014$. The solid angle factor is $\Omega/4\pi=7.75 \times 10^{-5}$ and other factors appearing in the equation at the 3.3 keV x-ray energy are $\epsilon_{CCD}=0.75$ and $T_{WINDOW}=0.64$. The theoretical value for the spectrometer efficiency is therefore to be $\epsilon=5.2 \times 10^{-7}$ in good agreement with the experiment, implying that the spectrometer has been well aligned and in this experiment performing close to its optimum.

A more general expression for the spectrometer efficiency is given in terms of its response to an arbitrary source E_λ , which in the case of a plasma will be the volume emissivity (photons $\text{cm}^{-3} \text{s}^{-1}$) and Δz is the emitting plasma depth

$$N = \kappa \frac{W}{R} \psi_y R_c R \sin \theta H \epsilon_\lambda t \left[\frac{E_\lambda \Delta z}{4\pi} \right],$$

where the expression in brackets is the line or continuum radiance. The product of $\psi_w=W/R$ and ψ_y , the viewing angles in the plane and perpendicular to the plane of dispersion, represents the solid angle subtended by the crystal. The product $(R_c \cdot R \sin \theta \times H)$ is the effective slit aperture to monochromatic radiation. Using the convention that the spectrometer “throughput” in units of $\text{cm}^2 \text{sr}$ is a product of the slit aperture and the solid angle subtended by the diffraction element, then $(W/R) \cdot \psi_y \cdot R_c R \sin \theta H$ is the “throughput.” ϵ_λ is the overall efficiency of the windows, filters, and CCD. The factor $\kappa = \psi_w / (\theta_1 - \theta_2)$, where $\psi_w = W \sin \theta / R \sin \theta$ and $(\theta_1 - \theta_2)$ is the band pass, is introduced¹⁴ to take into account the ‘filling factor’ of the instrument F/no. where the spatial dimensions of the source do not satisfy the band pass considerations. In the earlier expression, above, used for the EBIT theoretical efficiency ϵ , the factor $\epsilon_{CRYSTAL}$ is essentially $\kappa \cdot \langle P_C(\lambda) \rangle$ where $P_C(\lambda)$ is the Prins function.

III. CCD DETECTOR

A. Quantum efficiency

The CCD detector system adopted for the Johann spectrometer was developed by the X-ray Astronomy Group at the University of Leicester.³⁹ The CCD chip, manufactured by EEV Ltd.,⁴⁰ has 1152 (vertical) \times 1242 (horizontal), 22.5 μm square pixels, giving a total imaging area of $26 \times 28 \text{ mm}^2$. Early experiments with the spectrometer, reported by Abbey *et al.*¹¹ used a 2 kV silicon chip, the relatively high resistivity giving a greater depletion depth and higher quantum efficiency in the 5–10 keV range. The quantum efficiency (QE) of the detector is shown as a function of energy in Fig. 19 and peaks at $\sim 80\%$ at 4 keV. The narrow feature at 1.8 keV is the K-absorption edge of silicon. How-

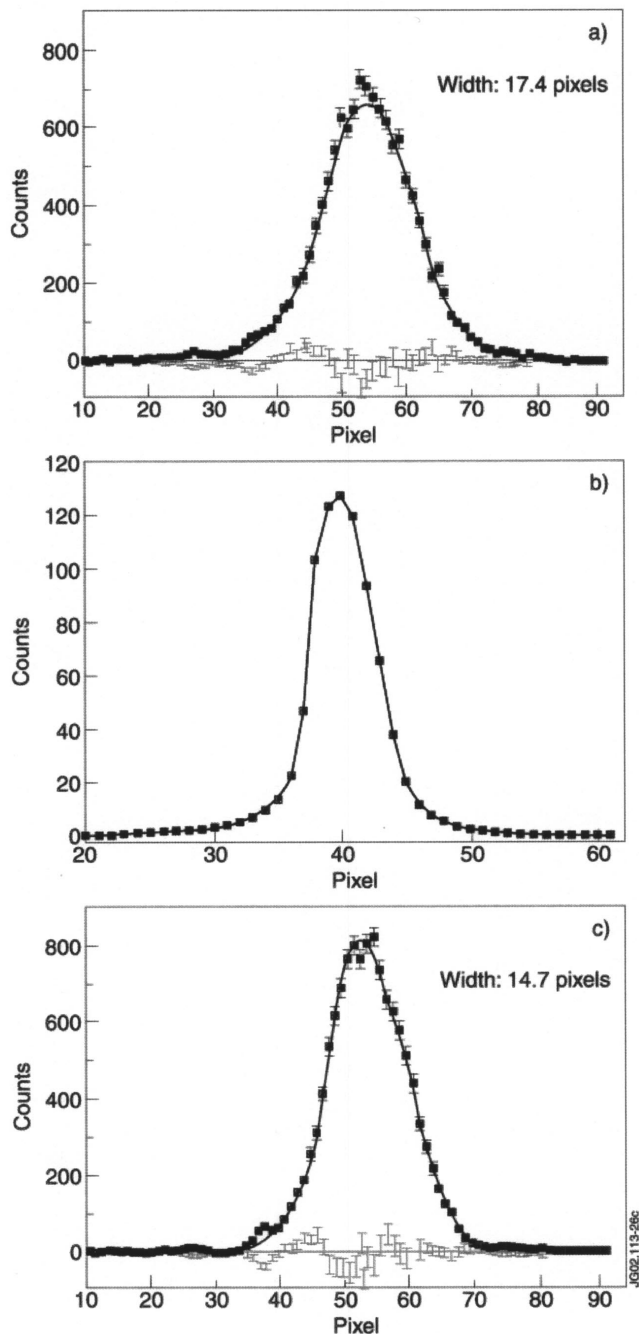


FIG. 18. (a) The $\text{Ly-}\alpha_1$ component of Ar^{17+} with EBIT source close to the Rowland circle of the Johann spectrometer. (b) Calculated point spread or instrument function for $\text{Si}(111)$ crystal using “Virtual Johann” ray tracing code (Ref. 36). (c) Deconvolution of the data in (a) using the instrument profile in (b). The “best fit” continuous lines shown are all Gaussian.

ever, since most of the Tokamak results, presented hereafter in Secs. III and IV, pertain to photon energies $\varepsilon \leq 4$ keV, a more easily obtainable CCD made on low-resistivity silicon ($25 \Omega \text{ cm}$) has often been used. This CCD, EEV 05–30 has a QE of $\sim 60\%$ at 3 keV.

The CCD is mounted on a copper cold finger and in operation the CCD is cooled either using liquid nitrogen or a two-stage thermoelectric cooler. Liquid nitrogen cooling is applied by connecting a cold feed (at liquid nitrogen temperature) to the CCD cold finger via a thick copper braid. The CCD temperature is actively controlled, using a PRT and

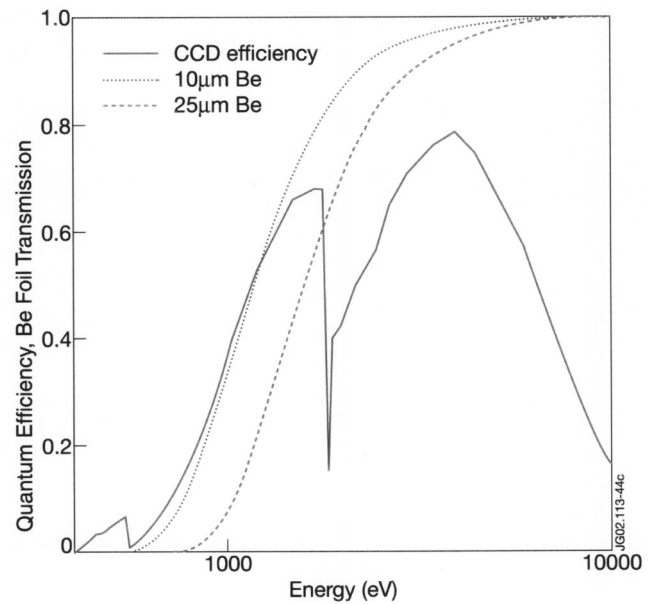


FIG. 19. Quantum efficiency of CCD detector as a function of energy. Transmissions through grid-supported Be windows of thickness 25 and $10 \mu\text{m}$ are also indicated.

a resistive heater to -100°C . When using TEC cooling, no active control is applied and the minimum operating temperature is typically -40°C . The CCD is attached to a “floating” printed circuit board (PCB) which contains a pre-amplifier and low-pass filters for the supply voltages. Electrical connection to the CCD itself is made via thin wires that provide a thermal break between the cooled CCD and the PCB. Typical read noise, at -100°C , is 5 electrons rms.

The energy required to create an electron–hole pair in silicon is 3.65 eV, yielding an inherent energy resolution,⁴¹ determined by Fano statistics and electronic noise of $\Delta E \sim 150$ eV. The detector is therefore an energy dispersive spectrometer on its own right and is capable of single photon detection. For example, absorption of an $\text{Ar Ly-}\alpha_1$ photon with 3.32 keV energy will produce an equivalent charge of about $500 \pm (5-10)$ electrons/pixel with a resolving power of approximately 20. A pixel “well” can comfortably accommodate 10^5 electrons of charge for transfer to its neighbor, implying a saturation level per pixel of ~ 200 $\text{Ar Ly-}\alpha_1$ photons. A pulse height spectrum of the full chip image or a portion of it as indicated in Fig. 20, will typically show⁹ several peaks, the lowest energy peak corresponding to detector pixels that do not contain x-ray events, the second due to single photon events, the third due to double photon absorption, and further peaks due to spurious lines and higher order events. Background radiation, such as that due to runaway electrons in the plasma, appears as a quasiexponential continuum, and peaks due to fluorescence of the crystal are sometimes observed.

A preliminary analysis of a full-frame exposure is extremely useful¹⁴ in determining the alignment of the spectral lines and in noise subtraction. It is recommended, during operation, to supply “noise thresholds” as indicated in the EBIT spectra of $\text{Ar Ly-}\alpha_1$ in Fig. 21. An event whose analog to digital converter (ADC) value falls below the lower en-

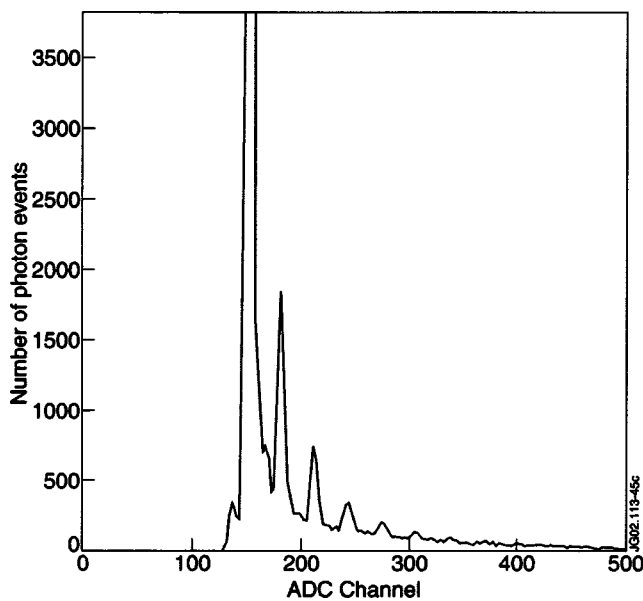


FIG. 20. Pulse height spectrum from COMPASS-D shot No. 14977 (time resolved mode). The first peak at 160 on the ADC scale is background noise level with a width ~ 150 eV. The peak at 190 is the Cl line at 2793 eV. Subsequent peaks indicate multiple photon events. The ADC count scale can be fitted to an energy scale by exposure of the chip to 5.9 keV photons from an ^{55}Fe source.

ergy value is rejected as noise. For every pixel containing an event above the lower threshold, the pixel co-ordinate and ADC (channel) value is stored and can be used to optimize the signal/noise as illustrated for the ArLy- α_1 line in Fig. 21(d). The ADC channel scale can be fitted to an energy scale by exposure of the chip to a low flux of 5.90 keV Mn K x-ray photons from an ^{55}Fe source. The ^{55}Fe calibration source is fixed in position within the diffraction arm and filtered so as to give a count rate of a few counts per second integrated over the full array. This is sufficient to give an energy calibration, while being negligible relative to the high count rates produced during the Tokamak discharge. In the case of exposures to EBIT the ^{55}Fe source can be switched off by pointing the source away from the detector.

B. Readout modes

Most CCD devices used for x-ray spectroscopy are three phase, frame-transfer devices. The solid state structure of the CCD, which is essentially a 2D array of coupled, pixel-size capacitors, the bias voltages required for the pixel to accumulate charge and the clocking sequences of potentials, which transfers or “couples” the charge on an individual pixel to its immediate neighbor, are described by Fraser.⁴¹ In the applications described here, all the detector functions, including temperature control, setting of bias voltages, readout sequences, and data acquisition are controlled via CAMAC by an Acorn RISC-PC. Different sizes of array and various readout modes can be programmed by downloading an appropriate sequence to the CAMAC sequencer module, which then runs the sequence continuously, or in response to an external trigger via CAMAC. Software for data display and analysis is available on the RISC-PC, with the time-

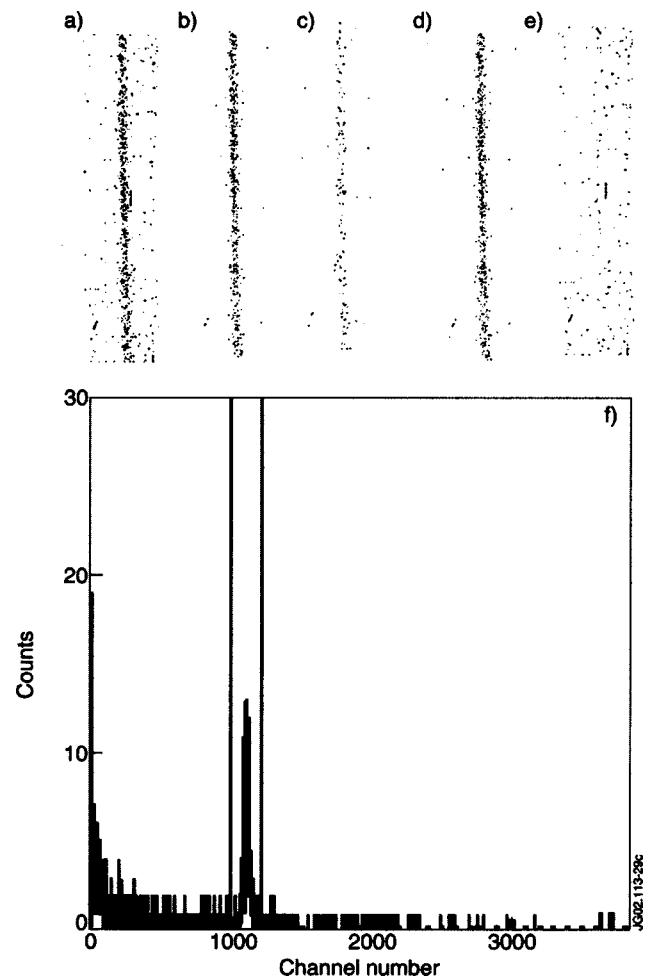


FIG. 21. CCD data processing of the Ly- α_1 component of Ar $^{17+}$ in an EBIT source: (a) raw data showing ALL counts above noise threshold; (b) one pixel events within thresholds; (c) two pixel events within thresholds; (d) one and two pixel events within thresholds; (e) all the events outside thresholds; and (f) histogram showing locations of upper and lower thresholds on energy scale.

critical array manipulations being coded in assembly language.

Two main readout modes have been used: either a 2D mode, where the result of each integration time is read out as a 2D “photographic” image, as in Fig. 21, or a 1D mode, where the 2D image of each time frame is compressed on the chip itself. The CCD transfer or “coupling” time between the charge on an individual pixel to its immediate neighbor is $\sim 2 \mu\text{s}$. The full-frame transfer time, that is the transfer of pixel charge, row by row, along the pixel columns and finally into a storage region, the last row of which is finally read out serially and digitized using a 12-bit ADC operating at 50 kHz, can take several, even tens of seconds. The ADC integration time can be varied from as short as 1 to 10 μs by software commands allowing some tradeoff between time resolution and read-out noise.

For maximum sensitivity in low-flux applications, the full area of the CCD may be exposed, and read out as an 1152×1242 array. Since the image is being swept across the array during readout, this full-frame mode is only useable in low count-rate applications requiring integration, or exposure, times of a minute or more, to avoid significant crosstalk

between frames. In the case of exposure to an EBIT source the transfer time gives negligible distortion to the overall image which may have been exposed, typically for over a fraction of an hour or longer. This mode is important therefore for low flux and possibly high background sources common to beam-foil, beam-gas, and ion-trap experiments, where the low readout noise allows long integration times, and the energy resolution gives good background rejection.

The frame-transfer 2D mode is routinely used in these experiments as a diagnostic check of the spectrometer alignment and optimizing signal-to-noise ratio, Fig. 21, particularly after any change in the instrument setup. The 2D image of spectral lines allows a partial check of the optical alignment, where a vertical tilt error of the crystal results in uneven intensity along the height of the line. Errors in the rotational adjustment of the detector about the normal to its surface cause the spectral lines to be nonparallel with the columns on the array. This can be allowed for in a 2D image, but leads to spurious line broadening when the image is vertically compressed on the chip. Inspection of the 2D image allows the detector tilt to be adjusted as necessary. Improved time resolution with negligible interframe smearing can be achieved by masking the frame-store half of the array, and operating in frame-transfer mode. At the end of each integration period the 2D image on the active area is transferred in about 1 ms onto the frame-store region, to be read out during the next integration period. This mode can operate continuously with a frame time of about 3 s and was useful for commissioning the instrument on a long pulse device such as JET, giving a series of 2D images with full energy information.

To deal quantitatively with count rates typical of high-flux sources such as a Tokamak plasma, it is necessary to sacrifice the inherent energy resolution by collecting multiple photons per pixel. In this alternative readout mode, one half of the CCD array is used to collect photons, the other half, the frame store half, is covered by an aluminum mask and is used for storage. After successive integration periods, the total charge in each pixel column is binned down and the integrated charge versus pixel position or histogram is stored on single adjacent rows of the frame store half. A time resolution ~ 1 ms is possible for this operation. When the frame store is full, each storage row yields a dispersed spectrum. The frame store, typically containing 500×1 ms slices of data can then be read out *a posteriori*. The time sequence can be recomposed as a streak record, as illustrated in Fig. 22. This is our usual mode of operation with Tokamaks. The spectrometer was installed on the JET Tokamak initially for only 1 day to assess the performance of the time-resolving mode of the CCD array. A Si(111) crystal, $2d = 0.6271$ nm, was bent to a radius of 997 mm and set up to observe the time-resolved spectrum of He-like Cl XVI, shown in Fig. 23. The frame-store half of the CCD array was masked, as above, and the open area was protected against visible light by a graphite-coated $2 \mu\text{m}$ Mylar filter. A preliminary, single exposure was made where the full 2D image was saved, in order to check the position of the image on the CCD array, and the alignment of the spectral lines with the pixel columns, necessary for on-chip compression. All other dis-

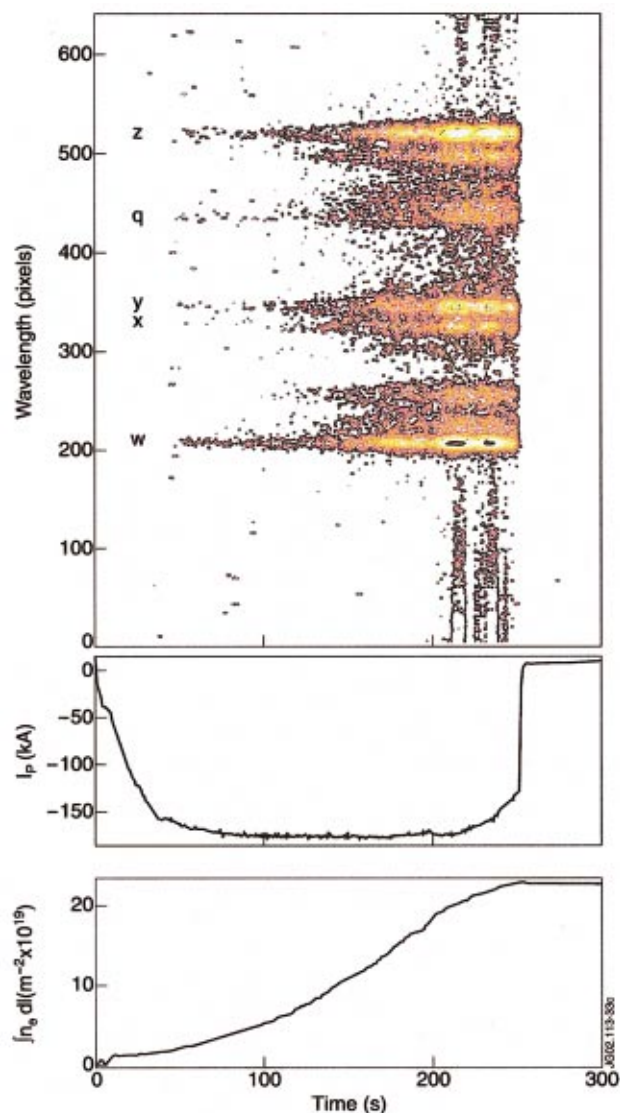


FIG. 22. (Color) Streak image of the time-resolved spectrum of Cl XVI from COMPASS-D discharge No. 13449 using the Johann CCD spectrometer. Notation of the lines as adopted by Gabriel (Ref. 42). The chlorine intensity increases monotonically towards the end of the discharge.

charges, as in Fig. 23, were recorded using the on-chip binning mode, which gave a time resolution of 40 ms for the discharge duration of about 23 s.

For long-lived plasmas as on JET, the charge distribution generated on a smaller chip size, 1024×256 , can be clocked down directly onto the readout register with a frequency of ~ 3 Hz. This readout mode gives a continuous monitor of the spectrum during the full duration of the pulse.

For an extremely intense source such as a synchrotron, a time resolution of $\sim 100 \mu\text{s}$ could in principle be achieved by masking all but a single row on the array, and operating in a quasistreak-camera mode.

IV. APPLICATIONS OF JOHANN SPECTROMETER

The group of x-ray lines from H-like and He-like ions due to $n = 2 - 1$ transitions with their associated satellite lines involving additional screening electrons, makes an ideal bandwidth to investigate with the Johann spectrometer. As

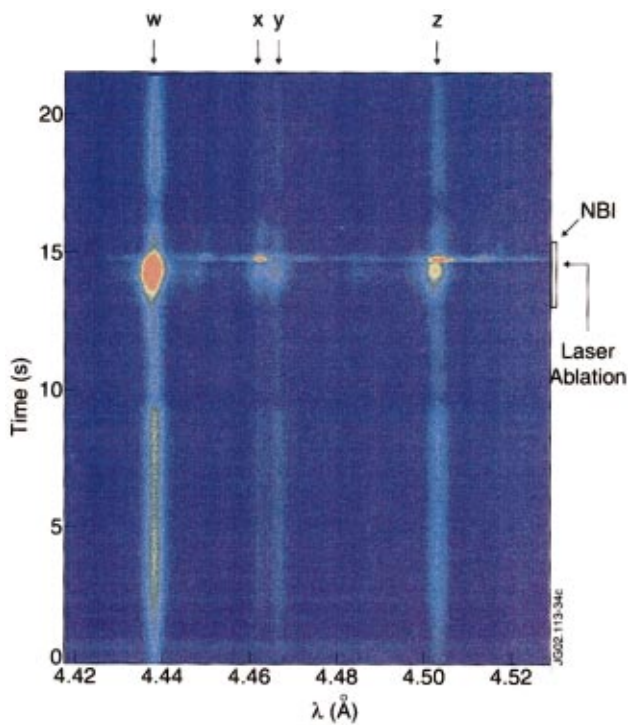


FIG. 23. (Color) False-color spectrum of Cl XVI ion emission during JET discharge. Lines are annotated using notation adopted by Gabriel (Ref. 42): $w = 1s^2\ ^1S_0 - 1s2p\ ^1P_1$, $x = 1s^2\ ^1S_0 - 1s2p\ ^3P_2$, $y = 1s^2\ ^1S_0 - 1s2p\ ^3P_1$, $z = 1s^2\ ^1S_0 - 1s2s\ ^3S_1$. Each horizontal row results from compressing the 2D image onto a single line of the frame-store region of the CCD. The time resolution is 40 ms. A Doppler blueshift, caused by toroidal plasma rotation, is visible during neutral-beam injection. A mixture of Mo and Ge is injected into the plasma by laser ablation, causing several transient lines to be recorded.

we will demonstrate below, this group of emission lines contains a wealth of diagnostic information without the need for relative efficiency calibration within the narrow pass band. In the spectra from K-shell ions with $Z > 12$, the $1s^2\ ^1S_0 - 1s2p\ ^1P_1$, $1s2p\ ^3P_{1,2}$, $1s2s\ ^3S_1$, transitions become interspersed with a rich spectrum of dielectronic lines and inner-shell excited lines of the type $1s^2nl - 1s2pnl$, where the nonparticipating or “spectator” electron, or electrons, have quantum states $nl \geq 2$.

The theory determining the wavelengths and intensities of these lines was outlined by Gabriel⁴² as early as 1972 but has subsequently been refined and improved over a sequence of articles by several authors, as described in reviews on “Fusion Spectroscopy.”^{43,44} Extensive diagnostic analyses of the $n = 2 - 1$ x-ray transitions throughout the isoelectronic sequences from Ne IX through Kr XXXV have now been made in the field of Tokamak x-ray spectroscopy. Reviews of some of these Tokamak studies are given by Bitter *et al.*⁴⁵ (1993) and Bartiromo⁴⁶ (1986).

We illustrate the diagnostic potential of the satellite spectra by reference to the Cl XVI emission from the JET and COMPASS Tokamaks in Fig. 24, where the energy levels and annotations of the main emission lines are shown. A self-consistent derivation of the parameters of electron and ion temperatures, density and poloidal, and toroidal fluid velocities T_e , T_i , n_e , $V_{\theta, \phi}$, respectively, can in principle be derived from the Cl emission within the narrow spectral re-

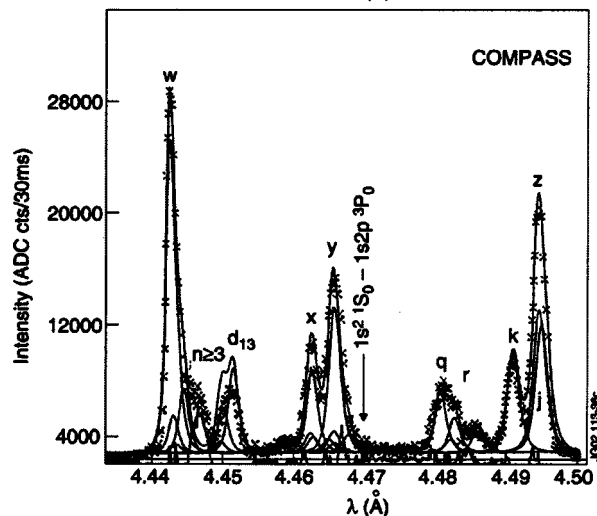
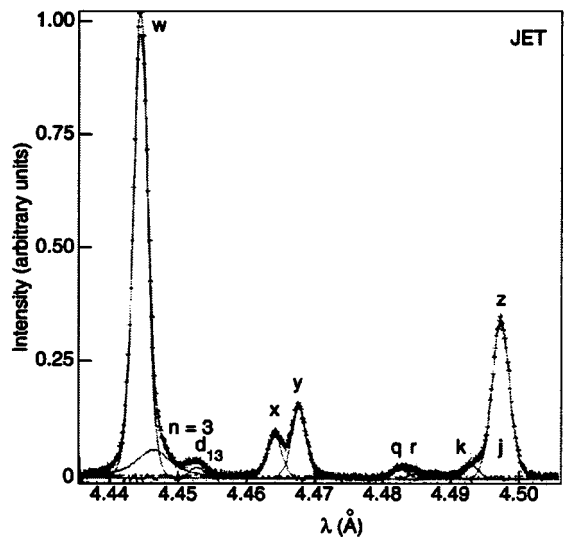
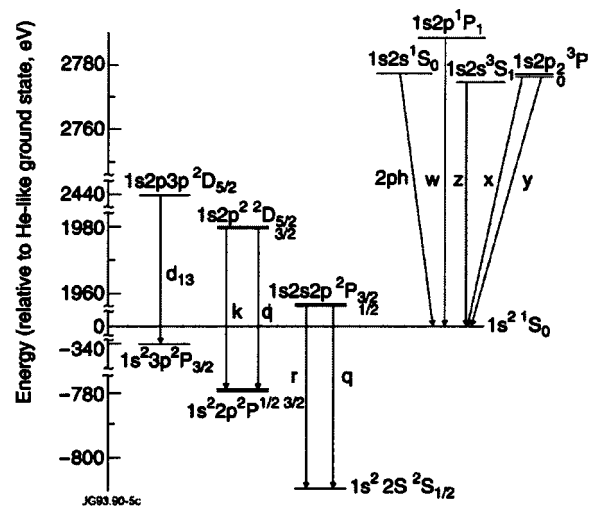


FIG. 24. Comparison of $n = 1 - 2$, Cl XVI spectrum and associated satellites from JET (top) and from COMPASS_D (bottom). The lower electron temperature ($T_e \leq 1$ keV) in the COMPASS Tokamak is evidenced by the prominence of the dielectronic satellites relative to those in the JET ($T_e \geq 1$ keV) spectrum. Energy levels and annotations for the transitions studied are also shown.

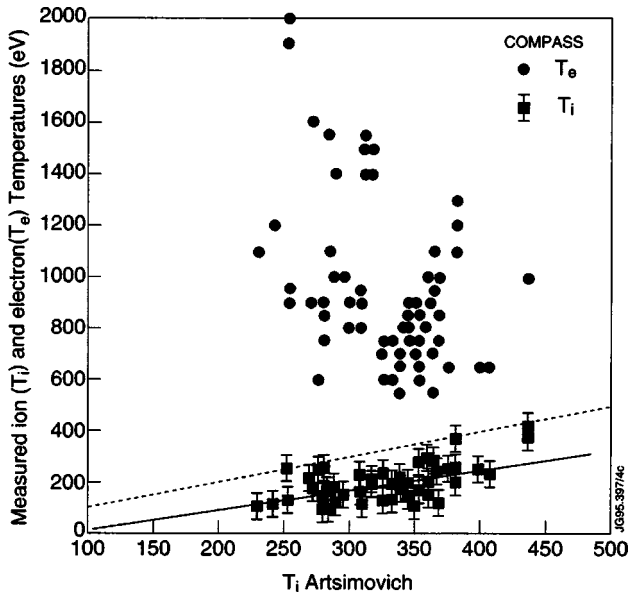


FIG. 25. Electron and ion temperatures derived from analyses of COMPASS-D spectrum of Cl XVI. Line intensity ratios d_{13}/w and k/w are used to derive T_e while line profiles of the blue wing of the w line are used for T_i . The lower group of points (<450 eV) refer to T_i while the upper group (>450 eV) refer to T_e . T_i scaling due to Artsimovich (Ref. 49) is shown as a broken line while the solid line is the best fit to the T_i data.

gion from $4.44 \rightarrow 4.50 \text{ \AA}$. The lower electron temperature $T_e \leq 1 \text{ keV}$ in the COMPASS Tokamak is evidenced by the prominence of the dielectronic satellites relative to those in JET, where the recombination satellite lines are weak relative to the (w, x, y, z) resonance lines. The Cl XVI emission shell is located on the flanks of the $T_e(r)$ profile on JET (minor plasma radius, $a = 1 \text{ m}$) at $(r/a) \approx 0.4$ where, typically, T_e could be a few keV. In COMPASS, the central electron temperature [$T_e(o) \approx 0.8 \text{ keV}$ and $a = 0.2 \text{ m}$] and Cl XVI is a core ion. In both cases, the location of the ions is determined by diffusive equilibrium.

The G ratio $[(x+y+z)/w]$ is nearly density independent for Cl XVI in Tokamaks^{47,48} but is temperature sensitive due to the different behavior of the singlet and triplet excitation rates. The R ratio $[z/(x+y)]$ is of limited interest in Tokamaks since it will only show density dependence, due to collisional de-excitation of the metastable, $1s2s^3S_1$, above 10^{20} m^{-3} .

The ratios of the dielectronic satellites to the resonance line w , for example (k/w) and (d_{13}/w) , are conveniently independent of ionization balance and of electron density n_e but are steeply dependent on temperature T_e with the form

$$I(k)/I(w) \sim (T_e)^{-1} \exp[(E_w - E_s)/kT_e],$$

where E_w and E_s refer to excited state energies above the ground state of Cl XVI.

The ability to measure T_e (from the k/w ratio) and T_i (from the pseudo-Voigt function applied to unblended lines) simultaneously on a 10 ms time scale in COMPASS, allows an investigation of the heat transport, in particular the electron-ion transfer rate. Figure 25 shows the measured values of T_e against the corresponding value of T_i in COMPASS. The T_i measurements are compared with scaling relations suggested by Artsimovich (1972).⁴⁹ The measured

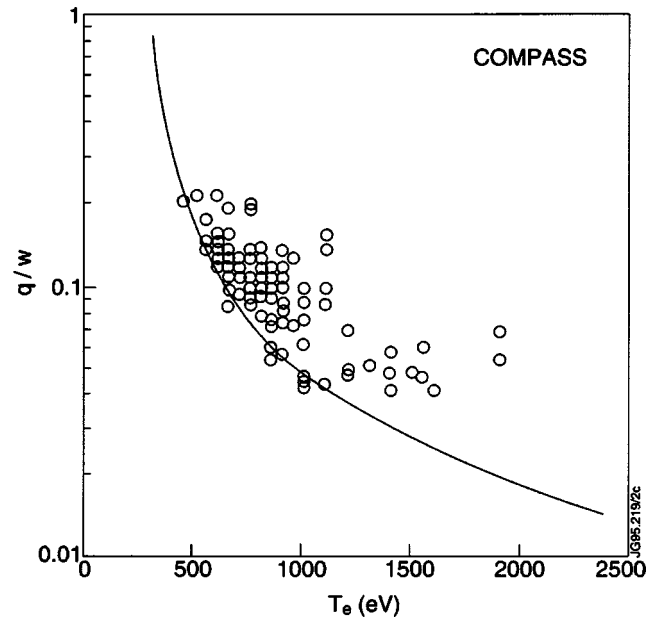


FIG. 26. The theoretical ratio of “ q/w ” line intensities in the Cl XVI spectrum plotted (full line) as a function of T_e . Coronal equilibrium values for N(Li-like)/N(He-like) have been used in the calculation. Experimental points from COMPASS-D are shown (circles) and lie above the coronal value, implying diffusive ion transport.

values are in general slightly lower than the predictions but increase with parameter values, particularly n_e , as expected. The T_e values, which are in general agreement with Thomson scattering, apply to all data for $T > 400 \text{ eV}$. The tendency for the temperatures of the ion and electron fluids to come together at higher values of the Artsimovich parameter, proportional to $(n_e)^{1/3}$, can be understood in terms of the electron power balance.

The satellite lines produced by inner-shell excitation from the ground states of Cl XV, on the other hand, have nearly the same excitation function as for the resonance line w , so the ratio

$$(q/w) \approx N(\text{Cl XV}) \cdot f_q \cdot A_r / N(\text{Cl XVI}) \cdot f_w \cdot \Sigma(A_r + A_a),$$

where A_r and A_a are the radiative and autoionizing decay rates, respectively, of the $1s2s2p$ levels, is nearly independent of T_e and measures the ionization balance or departures from it. Ion diffusion will also alter the (Li-like/He-like) ion abundance ratio as indicated by the (q/w) line ratio, both lines being excited from the ground states of the respective ions. Coronal balance is a lower bound to the data set of (q/w) ,⁵⁰ the largest departure from coronal being found, as illustrated in Fig. 26, at the highest T_e , and consequently lowest n_e , where anomalous (see below) diffusive processes are relatively rapid. We have chosen Cl ions preferentially since chlorine is a relatively common intrinsic impurity in Tokamaks. A more manageable test atom, which can be introduced in a controlled manner to diagnose the local plasma parameters and test models of ion transport, is argon. The spectral signature of ionized Ar is isoelectronic with that from chlorine as illustrated by the Ar XVII spectrum from JET in Fig. 27. Enhancement of the population of the $n = 2$ triplet states in Ar XVII relative to the singlets due to local recom-

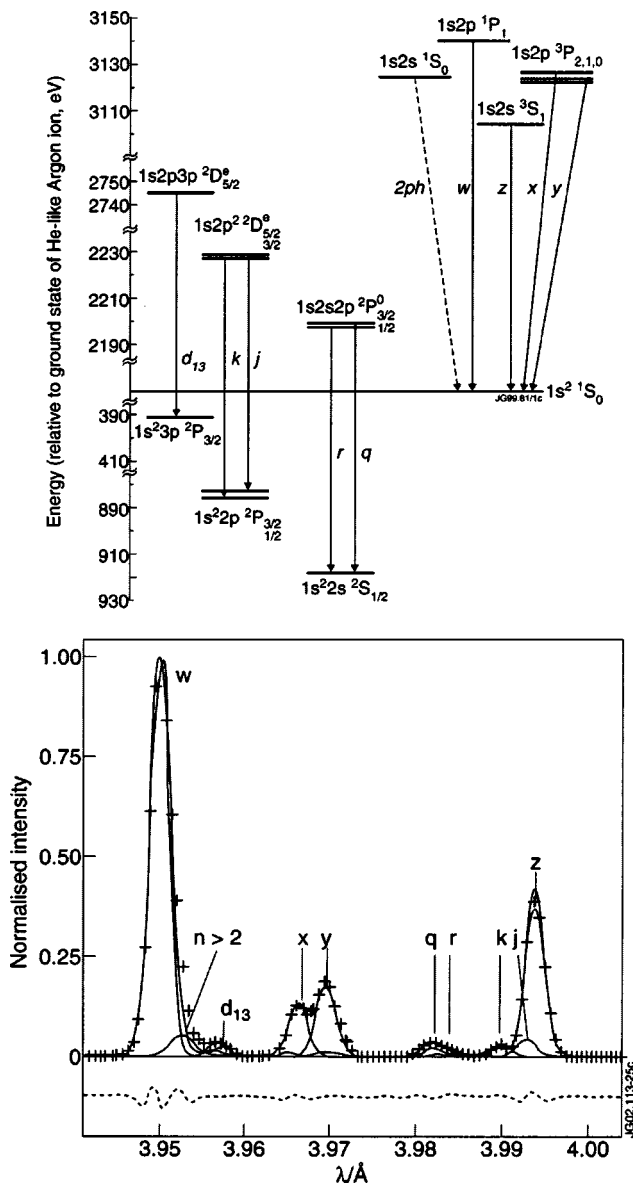


FIG. 27. Energy levels and transitions (above) of $n=1-2$ transitions in Ar XVII and associated satellites of Ar XVI. Spectrum from JET discharge No. 49704 at $t=10$ s with integration time of 10 ms. The best fit of the synthetic spectra to the experimental data and the residuals are also shown (bottom).

bination processes, such as charge exchange with neutrals near the plasma edge in Tokamak plasmas, has been noted by Källne *et al.*⁵¹

Changes in the temporal behavior and local intensities of spectral lines from ions injected as test species into the plasma can be interpreted in terms of ion transport. The background fuel ions and impurities are strongly linked by collisions in fusion plasma systems so that a study of the spectral emission from impurities directly yields information on the overall particle transport and often on the total plasma energy. Particle and energy transport in Tokamaks often behave similarly in many plasma operating conditions.

According to neoclassical theory, classical density and temperature gradient driven fluxes enhanced by the Tokamak geometry, cross-field particle diffusion,⁵²⁻⁵⁴ should be a slow process with diffusion coefficients $\sim 0.01 \text{ m}^{-2}$. Commonly, in most discharges exhibiting so-called *L* mode, i.e., im-

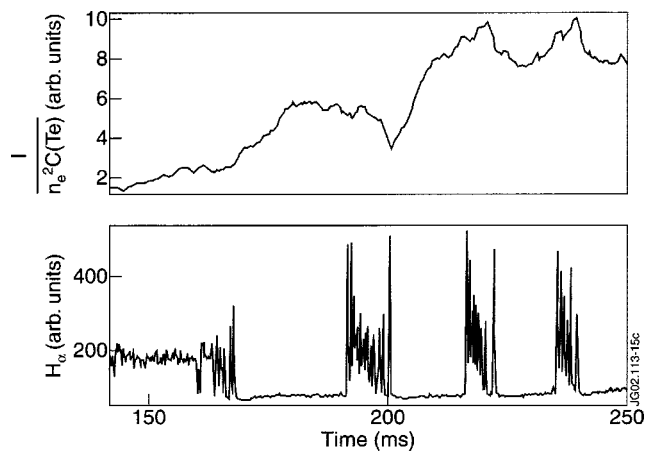


FIG. 28. Time history of the w line intensity of Cl XVI in COMPASS-D No. 13460 showing accumulation ($\times 2$) of Cl ion impurity concentration (top) during periods of enhanced particle confinement characterized by reduced edge recycling and low Balmer- α activity (bottom).

paired or “low” confinement or in (edge localized instability modes discharges), the cross-field diffusion coefficient will be some $50\times$ higher than neoclassical. In these *L* mode discharges the impurity line intensities mimic changes in the source strength or, more typically, follow changes in n_e , the electron density.

While neoclassical ion transport is not usually achieved in Tokamak experiments, in some operating scenarios, such as fueling the core by solid fuel pellet injection,⁵⁵ such impurity accumulation has been observed. Neglecting the temperature gradient terms, in the neoclassical limit, ambipolarity of the ions and electrons should cause a Z-dependent accumulation of impurities relative to the fuel ions, $n_i(r=0)$, corresponding to the peak value of $n_e(0)$ on axis

$$\frac{n_Z(r=0)}{n_Z(r=a)} = \left(\frac{n_i(r=0)}{n_i(r=a)} \right)^Z.$$

In the COMPASS plasmas such neoclassical effects are not achieved but modest accumulations of impurities^{9,34} in the core have been observed during periods of improved confinement. These are illustrated by the temporal intensity of the w line from Cl XVI as indicated in Fig. 28. Dividing the intensity by n_e^2 gives the fractional impurity concentration, i.e., the concentration as a fraction of n_e . Accumulation is then an increase in the fractional impurity concentration, assuming the source strength remains constant. In Fig. 28, accumulation ($\times 2$) of the Cl ion impurity concentration (upper) is indicated during periods of enhanced particle confinement characterized by reduced edge recycling and low Balmer- α activity (lower). Corrections⁹ to the w line intensity have been made to account for the small $\approx 5\%$ electron temperature rise during the *H*-mode periods.

Fluid rotation of fuel and impurity ion species is of some consequence in the construct of the radial and toroidal force balance on the species. The radial impurity pressure, for example, may be written as $\nabla P_Z = eZn_Z(E_r + V \times B)$. Components of the poloidal and toroidal velocities, $V_{\theta, \phi}$ can have very different magnitudes, however. The velocity of impurity ions driven toroidally by neutral beams as in JET can approach 10^6 ms^{-1} and the rotation is immediately obvious as

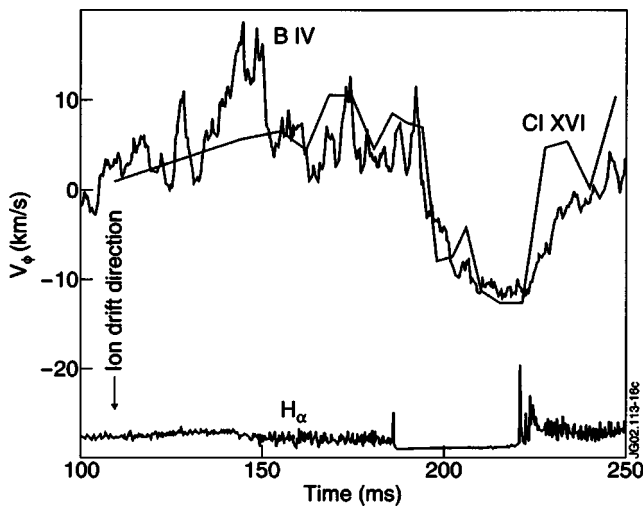


FIG. 29. Toroidal rotation (upper) derived from centroid shifts of core Cl XVI lines throughout COMPASS-D discharge No. 12570 and including H -mode period when the rotation increases in the ion drift (negative) direction. The rotation is normalized at 180 ms to rotation measured from Doppler shifts of near visible BIV lines near the plasma edge. The enhanced confinement H mode is defined by the quiescent period of H - α activity.

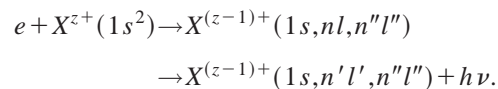
shown in Fig. 23. The poloidal velocity is usually much less, $V_{\theta} \leq 10^4 \text{ ms}^{-1}$ and places a higher requirement on the instrument resolution. Differential rotation at different plasma radii is relevant to the magneto hydrodynamic stability of Tokamaks. In general, fluid shear will stabilize the growth of instabilities. One example is the growth of island formation at the $q=2$ rational surface as a result of neoclassical tearing modes driven by saw-teeth instabilities at the $q=1$ surface. Figure 29 illustrates an attempt to compare core rotation derived from centroid shifts of Cl XVI lines throughout a COMPASS-D discharge, including an H -mode period when the rotation increases in the ion drift (negative) direction, with the Doppler shifts of near visible BIV lines near the plasma edge. The enhanced confinement H -mode period is defined as much by maximum fluid rotation as by quiescent H - α activity. In order to detect rotational shear between ad-

jacent rational surfaces of course, shifts in the centroids of x-ray lines from nearly adjacent impurity ion charge states would have to be measured.

A quite different application of the one- and two- electron spectra in Tokamaks has been the study of atomic structure. These ions are capable of precise *ab initio* calculations,^{21,56} including relativistic and quantum electrodynamics corrections to high order in Z , see, e.g., Mohr²¹ and Drake⁵⁶ for H- and He-like ions respectively. A comparison between theory and experiment in H-like high Z ions is given by Briand.⁵⁷ Precision crystal measurements of Ly $\alpha_{1,2}$ for Cl XVII at an accuracy approaching the 10 ppm level has been reported by Källne *et al.*²⁵ using the ALCATOR Tokamak. An alternative approach, recently followed by Tarbutt and Silver⁵⁸ using the present spectrometer to study Ti²¹⁺, is to use an EBIT source to generate H-like ion emission with low mass motion and thermal broadening. So far in these experiments, no systematic discrepancy between the most sophisticated theory and data, from the Tokamak and EBIT experiments, has been established.

A somewhat related observation^{8,25,59} is the Ly $\alpha_{1,2}$ intensity or β ratio which, in Tokamaks, is generally observed to exceed slightly the statistical ratio of 0.5. For $Z \sim 16$ or 17 as in these studies, it would appear that collisional and satellite effects contribute about equally to the departure of β from 0.5. At higher $Z > 20$, blending with the $M1$ decay of the $2s^2S_{1/2}$ excited state is expected to make a significant apparent increase in β .

In terms of atomic structure studies the EBIT source finds the most important role due to its controllable beam energy. This is particularly applicable to the study of doubly excited states populated predominately by the process of dielectronic recombination



The dielectronic process is state selective and is resonant in the incident electron energy, the free electron energy required

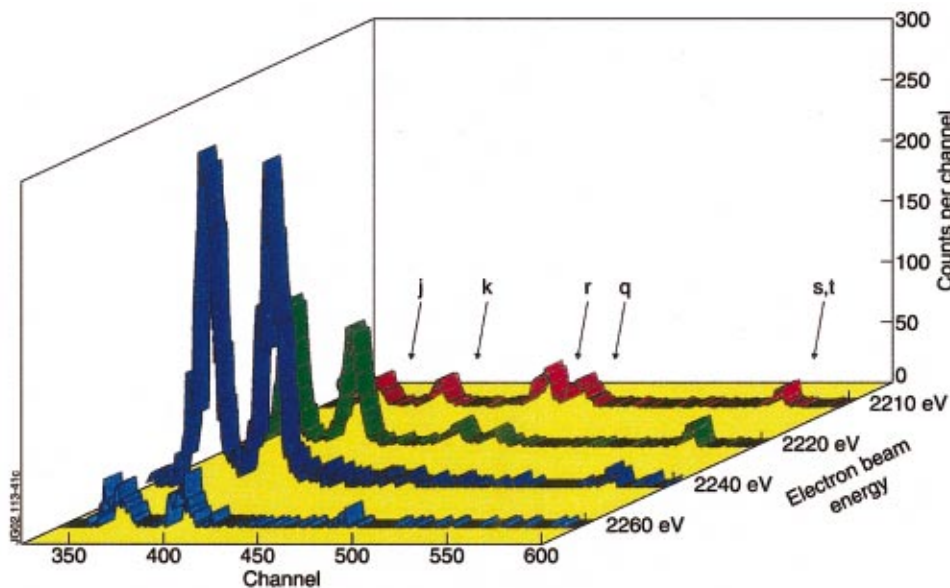


FIG. 30. (Color) Dielectronic excitation as a function of EBIT beam energy showing the $1s^22p-1s2p^2$ transitions excited around 2.24 keV and the $1s^22s-1s2s2p$ transitions around 2.21 keV.

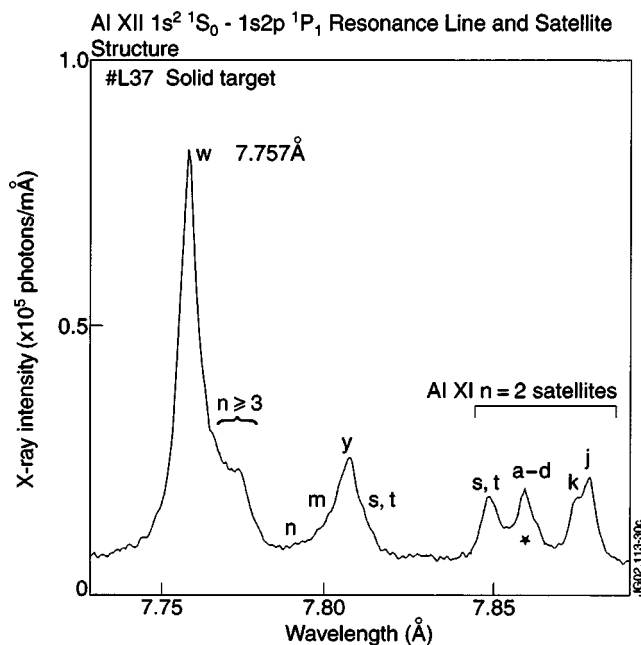


FIG. 31. Laser-produced plasma spectrum of $1s^2-1s2p$ transitions in Al XII and associated satellites. Notation due to Gabriel (Ref. 42).

being equal to the energy of the doubly excited state above the ground state energy of the He-like ion. If the electron beam energy is set below the threshold for exciting these transitions, no lines are observed. The beam energy has to coincide with a dielectronic resonance. As indicated in experiments³⁵ with the Oxford EBIT on the satellites to the $n=2$ resonance lines of Ar XVII, Fig. 30, the $1s2p^2$ states, corresponding to the j and k lines, are excited with the beam energy set at 2.24 keV, while at slightly lower (-30 eV) energy, the $1s2s2p$ states, corresponding to the r and q lines, are excited. These latter $1s^2s-1s2s2p$ transitions are the same, (Fig. 27) as observed above a threshold of 3.114 keV by direct impact excitation from the Li-like ion ground state but here excited dielectronically. The smearing of the satellites along the energy scale is due to the spread ≈ 20 eV in the beam energy.

Finally, in order to emphasize the range of plasma parameters amenable to diagnosis by the spectrometer, we recall the measurements⁸ on bandwidth, Sec. II D, using the laser-produced plasmas generated by the Rutherford Appleton Laboratory VULCAN laser. These experiments using targets with “marker” layers were performed in order to derive localized electron densities from Stark broadened line profiles and from the density sensitive line intensity ratios of the Al XI dielectronic satellites to the Al XII $1s^2-1s2p$ resonance line at 0.7757 nm, Fig. 31. For this observation the crystal jig and film holder were mounted to an optical bench inside the laser target chamber. The target in this case was a solid 1 mm diam Al target. The spectrum was recorded on film from a single laser pulse (7 J, 20 ps, $\lambda = 520$ nm), using a PET(002) ($2d = 0.8742$ nm) crystal at a radius of 300 mm. In this spectrum, the line profiles are mainly Lorentzian due to Stark broadening, and the forbidden line z , present in the Tokamak spectrum, is absent due to collisional de-excitation at high density.

V. DISCUSSION

The form of construction and compact nature of this instrument have enabled high quality results to be obtained from a wide range of highly ionized laboratory sources. The incorporation of an x-ray CCD detector with several programmable operating modes has greatly increased the suitability of the instrument for a large variety of both high-flux and low-flux experiments.

ACKNOWLEDGMENTS

This work is partly supported by EURATOM and the U.K. Department of Trade and Industry.

Presented at the Proceedings of the 14th Topical Conference on High-Temperature Plasma Diagnostics, Madison, Wisconsin, 8–11 July 2002.

- ¹E. Källne and J. Källne, Phys. Scr., T **T17**, 152 (1987).
- ²K. W. Hill *et al.*, Rev. Sci. Instrum. **56**, 1165 (1985).
- ³R. Bartiroma, R. Giannella, M. L. Apicella, F. Bombarda, S. Mantovani, and G. Pizzicaroli, Nucl. Instrum. Methods Phys. Res. **225**, 978 (1984).
- ⁴R. Bartiroma, F. Bombarda, R. Giannella, S. Mantovani, L. Panaccione, and G. Pizzicaroli, Rev. Sci. Instrum. **60**, 237 (1989).
- ⁵P. Platz, J. Ramette, E. Belin, C. Bonnelle, and A. H. Gabriel, J. Phys. E **14**, 448 (1981).
- ⁶E. Källne and J. Källne, Phys. Scr., T **T3**, 185 (1983).
- ⁷R. Barnsley, U. Schumacher, E. Källne, H. W. Morsi, and G. Rupprecht, Rev. Sci. Instrum. **62**, 889 (1991).
- ⁸J. Dunn, Ph.D. thesis, University of Leicester, 1990.
- ⁹I. M. Melnick, Ph.D. thesis, University College, London, 1995.
- ¹⁰A. D. Holland, Nucl. Instrum. Methods Phys. Res. A **377**, 334 (1996).
- ¹¹A. F. Abbey, R. Barnsley, J. Dunn, S. N. Lea, and N. J. Peacock, in *UV and X-ray Spectroscopy of Laboratory and Astrophysical Plasmas*, edited by E. Silver and S. Khan (Cambridge University Press, Cambridge, 1993), p. 493.
- ¹²N. J. Peacock, M. H. Hughes, H. P. Summers, M. Hobby, M. W. D. Mansfield, and S. J. Fielding, *Proceedings of the 7th International Conference, Innsbruck, Austria, August 1978* (IAEA, Vienna, 1979), Vol. 1, pp. 303–314.
- ¹³I. H. Coffey, Ph.D. thesis, Queen’s University of Belfast, Belfast, Ireland, 1993.
- ¹⁴M. R. Tarbutt, Ph.D. thesis, Clarendon Laboratory, University of Oxford, Oxford, 2001.
- ¹⁵H. H. Johann, Z. Phys. **69**, 185 (1931).
- ¹⁶B. P. Duval, J. E. Bateman, and N. J. Peacock, Rev. Sci. Instrum. **57**, 2156 (1986).
- ¹⁷B. P. Duval, Ph.D. thesis, Clarendon Laboratory, University of Oxford, Oxford, 1986.
- ¹⁸R. Barnsley, Ph.D. thesis, University of Leicester, 1993.
- ¹⁹J. M. Laming, J. D. Silver, R. Barnsley, J. Dunn, K. D. Evans, and N. J. Peacock, Phys. Lett. A **126**, 253 (1988).
- ²⁰G. W. F. Drake (private communication, 1987).
- ²¹P. J. Mohr, At. Data Nucl. Data Tables **29**, 453 (1983).
- ²²J. D. Garcia and J. E. Mack, J. Opt. Soc. Am. **55**, 654 (1965).
- ²³J. Dunn, R. Barnsley, K. D. Evans, N. J. Peacock, G. J. Tallents, P. A. Norreys, and M. H. Key, J. Phys. (Paris) **50**, 551 (1989).
- ²⁴R. A. Hall, Ph.D. thesis, University of Leicester, Leicester, 1980.
- ²⁵E. Källne, J. Källne, P. Richard, and M. Stockli, J. Phys. B **17**, L115 (1984).
- ²⁶A. Burek, Space Sci. Instrum. **2**, 53 (1976).
- ²⁷M. Lewis, Ph.D. thesis, University of Leicester, Leicester, 1982.
- ²⁸R. Caciuffo, S. Melone, F. Rustichelli, and A. Boeuf, Phys. Rep. **152**, 1 (1987).
- ²⁹R. Caciuffo, C. Ferrero, O. Francescangeli, and S. Melone, Rev. Sci. Instrum. **61**, 3467 (1990).
- ³⁰A. E. Sändstrom, in *Handbuch der Physik*, edited by S. Flügge (Springer, Berlin, 1957), Vol. 30, p. 78.
- ³¹B. L. Henke, E. M. Gullikson, and J. C. Davies, At. Data Nucl. Data Tables **54**, 181 (1993).
- ³²J. Tudor Davies and J. M. Vaughan, Astrophys. J. **137**, 1302 (1963).

- ³³R. D. B. Fraser and E. Suzuki, in *Biological Applications*, edited by J. A. Blacburn (Marcel Dekker, New York, 1970), Chap. 5.
- ³⁴J. A. Rainnie, Ph.D. thesis, Queen's University of Belfast, Belfast N. Ireland, U. K., 2001.
- ³⁵M. R. Tarbutt, R. Barnsley, N. J. Peacock, and J. D. Silver, *J. Phys. B* **34**, 3979 (2001).
- ³⁶M. R. Tarbutt, "Virtual Johann" (calculations, to be published 2003).
- ³⁷W. H. Richardson, *J. Opt. Soc. Am.* **62**, 55 (1972).
- ³⁸L. B. Lucy, *Astron. J.* **79**, 745 (1974).
- ³⁹E. G. Chowanietz, D. H. Lumb, and A. A. Wells, *Proc. SPIE* **597**, 38 (1985).
- ⁴⁰EEV Ltd. (now Marconi Applied Technologies Ltd.), Chelmsford, Essex CM1 2QU, England.
- ⁴¹G. W. Fraser, *X-ray Detectors in Astronomy* (Cambridge University Press, Cambridge, 1989).
- ⁴²A. H. Gabriel, *Mon. Not. R. Astron. Soc.* **160**, 99 (1972).
- ⁴³N. J. Peacock, *Applied Atomic Collision Physics* (Academic, New York, 1984), Vol. 2, Chap. 5A, pp. 143–190.
- ⁴⁴N. J. Peacock, *Astrophys. Space Sci.* **237**, 341 (1996).
- ⁴⁵M. Bitter, H. Hsuan, K. W. Hill, and M. Zarnstropp, *Phys. Scr.*, T **T47**, 87 (1993).
- ⁴⁶R. Bartiromo, *Proceedings of International School of Plasma Physics*, Varenna, Italy, 1986; Course and Workshop on Basic and Advanced Diagnostic Techniques for Fusion Plasmas, EUR 10797 1986, Vol. 1, p. 227.
- ⁴⁷F. P. Keenan, S. M. McCann, R. Barnsley, J. Dunn, K. D. Evans, and N. J. Peacock, *Phys. Rev. A* **39**, 4092 (1989).
- ⁴⁸I. H. Coffey, F. P. Keenan, C. E. Adam, R. Barnsley, W. J. Dickson, K. D. Lawson, and N. J. Peacock, *Phys. Scr.* **47**, 169 (1993).
- ⁴⁹L. A. Artsimovich, *Nucl. Fusion* **12**, 215 (1972).
- ⁵⁰I. H. Coffey, R. Barnsley, F. P. Keenan, I. Melnick, P. McGinnity, M. G. O'Mullane, and N. J. Peacock, *Proceedings of 11th Colloquium on UV and X-ray Spectroscopy of Astrophysical and Laboratory Plasmas, Nagoya, 1995* (Universal Academy Press, 1996), p. 431.
- ⁵¹E. Källne, J. Källne, A. Dalgarno, E. S. Marmar, J. E. Rice, and A. K. Pradhan, *Phys. Rev. Lett.* **52**, 2245 (1984).
- ⁵²G. Fussmann, *Nucl. Fusion* **26**, 983 (1986).
- ⁵³G. Fussmann, IPP Report No. IPP 1/273, Habilitationsschrift, Max-Planck-Institute for Plasma Physics, Garching, 1992 (in German).
- ⁵⁴S. P. Hirshman and D. J. Sigmar, *Nucl. Fusion* **21**, 1079 (1981).
- ⁵⁵L. Lauro-Taroni, B. Alper, R. Giannella, K. D. Lawson, F. Marcus, M. Mattioli, P. Smeulders, and M. von Hellermann, *Proceedings on the 21st EPS Conference on Plasma Physics and Controlled Nuclear Fusion Research, Montpellier, 1994*, Vol. 18B, Part 1, p. 102.
- ⁵⁶G. W. Drake, *Can. J. Phys.* **66**, 586 (1988).
- ⁵⁷J. P. Briand, *Phys. Scr.* **46**, 157 (1993).
- ⁵⁸M. R. Tarbutt and J. D. Silver, *J. Phys. B* **35**, 1467 (2002).
- ⁵⁹J. M. A. Ashbourne, I. M. Melnick, and N. J. Peacock, *Phys. Rev. E* **65**, 066410 (2002).